Draft version August 15, 2026
Typeset using LaTeX **twocolumn** style in AASTeX631

Global fitting of quadrupolar mixed modes with near-degeneracy effects and their role in constraining stellar parameters

Meenakshi Gaira,[1] Sapnodip Pramanik,[2] Vishal Vetrivel,[3] Shravan Hanasoge,[1,4] and Shatanik Bhattacharya[1]

[1] *Department of Astronomy and Astrophysics, Tata Institute of Fundamental Research, Mumbai, 400005, India*
[2] *Department of Physical Sciences, Indian Institute of Science Education and Research, Kolkata, 741246, India*
[3] *UM-DAE Centre for Excellence in Basic Sciences, Mumbai, 400098, India*
[4] *Center for Space Science, NYUAD Institute, New York University Abu Dhabi, PO Box 129188, Abu Dhabi, UAE*

ABSTRACT

Quadrupolar mixed modes in evolved solar-like stars are significantly affected by near-degeneracy effects (NDE). However, owing to the weak coupling between the p and g modes, the g-dominated quadrupolar mixed modes have low visibility, and therefore, quadrupolar modes are often modeled as pure pressure modes. NDE alters their rotational splittings, resulting in asymmetric multiplets. Moreover, even in stars where NDE are weak, the rotational splittings of quadrupolar modes have a substantial contribution from core rotation; hence it is very important to characterize quadrupolar modes as mixed-modes. We perform a global asymptotic fit of the quadrupolar mixed modes of an early red giant KIC 7341231, incorporating near-degeneracy effects through an implicit formalism introduced by Li et al. (2024) to account for NDE in dipolar mixed modes. Using a Markov Chain Monte Carlo (MCMC) method to globally fit the oscillation spectrum obtained from *Kepler's* photometric data, we determine the quadrupolar mixed-mode parameters, including the coupling factor q_2, period spacing $\Delta\Pi_2$, gravity-mode phase offset $\epsilon_{g,2}$, and small frequency separation $\delta\nu_{02}$. We further investigate the utility of quadrupolar mixed modes in improving the constraints on stellar parameters. To this end, we perform Gaussian Process optimization(GPO)-based stellar modeling using the observed $\ell = 0, 1$ and 2 mode frequencies, along with the atmospheric observables $T_{\rm eff}$ and surface metallicity, as constraints. We compare the inferred stellar parameters obtained with and without the inclusion of quadrupolar modes. After including the quadrupolar modes, the best-fit mass, age, radius, initial helium fraction, and initial metallicity of KIC 7341231 change by 0.2%, 1.7%, 0.4%, 1.6%, and 0.2%, respectively. Additionally, the ranges of stellar parameters spanned by models satisfying our selection criterion do not change significantly. The lower bounds on mass, age and radius change by $< 0.5\%$, whereas the upper bounds change by 0.1%, 3.5% and 0.03%, respectively. These results suggest that, for evolved solar-like stars similar to KIC 7341231, with clearly identifiable and well-characterized dipolar mixed modes and no detectable acoustic glitch signatures, quadrupolar modes may only weakly improve constraints on stellar parameters beyond those provided by radial and dipolar modes.

1. INTRODUCTION

Quadrupolar mixed modes in evolved solar-like stars are often modeled as pure pressure modes in asteroseismic analyses, since the coupling between quadrupolar p and g modes is approximately an order of magnitude weaker than that for dipolar modes. However, their rotational splittings are substantially affected by near-degeneracy effects (NDE), which arise when the frequency spacing between successive mixed modes is comparable to or smaller than the rotational splittings (Deheuvels et al. 2017; Ong et al. 2022; Liagre et al. 2025; Li et al. 2024).

The coupling coefficient q_2 for quadrupolar modes is very small (see Table 5), and therefore, g-dominated quadrupolar mixed modes have much lower surface amplitudes, leading to poor visibility in the oscillation spectrum. However, these modes become visible when successive mixed-mode frequencies are sufficiently close that they lie within the avoided-crossing window (Deheuvels et al. 2017; Ong et al. 2022). In such cases, NDE modify the rotational splittings, resulting in asymmetric multiplets.

When quadrupolar mixed-modes are far from avoided-crossing windows, only p-dominated modes are visible. In this regime, their mixing fraction $\zeta(\nu)$ (ν is temporal frequency), defined as the ratio of the kinetic energy of the mode in the g-mode cavity to its total kinetic energy (Deheuvels, S. et al. 2015), is small ($\zeta(\nu) \lesssim 0.1$). Even in this case, a quadrupolar mode with $\zeta(\nu) \sim 0.05$ has about 5% of its energy in the core. For stars in which the core rotation rates are 10 times or larger than that of the corresponding envelopes, as is the case for most red giants (Li et al. 2024), the core rotation contribution to the overall rotational splitting is $\gtrsim 30\%$ (see Equation 18). Hence, for analyzing rotational splittings, quadrupolar modes should always be modeled as mixed modes. Correct characterization of rotational multiplets of quadrupolar mixed modes is important for putting constraints on latitudinal differential rotation and for investigating angular momentum transport mechanisms in evolved solar-like stars.

Modeling quadrupolar modes as mixed modes also yields additional seismic parameters – q_2, $\Delta\Pi_2$, $\epsilon_{g,2}$, and a precise estimate of the small separation $\delta\nu_{02}$ (these parameters are defined in Section 2). This work was motivated by the possibility that these additional seismic constraints could improve the modeling of stellar structure and thereby reduce the uncertainties in stellar parameters such as mass, age, radius, etc. Several studies have demonstrated the substantial impact of dipolar mixed modes in constraining stellar parameters (Wang et al. 2023; Pérez Hernández, F. et al. 2016; Li et al. 2017; Huber et al. 2019; Murphy et al. 2021). In this work, we investigated how quadrupolar mixed modes improve the constraints on stellar parameters beyond those already provided by the radial modes and dipolar mixed modes.

We performed a global fit of the quadrupolar mixed modes of an early red giant, KIC 7341231, using asymptotic theory. KIC 7341231 shows substantial NDE and has previously been analyzed by Deheuvels et al. (2017) and Liagre et al. (2025). We then carried out forward stellar modeling using Gaussian Process Optimization (GPO) to assess whether the additional seismic information provided by quadrupolar modes leads to tighter constraints on stellar parameters. For this analysis, we used the observed frequencies of all $\ell = 0, 1$ and 2 modes, together with atmospheric observables ($T_{\rm eff}$ and surface metallicity), as constraints. We analysed how the inclusion of quadrupolar modes changes the best-fit stellar parameters and the ranges of stellar parameters spanned by the top stellar models satisfying our selection criterion (Section 4.2.3).

In addition, the implicit approach introduced by Li et al. (2024) to account for NDE in dipolar mixed modes is applied here for the first time to quadrupolar mixed modes. Recently, Liagre et al. (2025) also performed a global fit of the quadrupolar mixed modes of the same star using a different methodology. The best-fit parameters we obtained here using the first approach are in good agreement with those reported by Liagre et al. (2025), with all values lying within the quoted error bars.

The approach introduced by Li et al. (2024) is conceptually similar to that proposed by Ong et al. (2022), who showed that the rotation operator is diagonal in the basis of uncoupled p and g modes. Consequently, the rotational perturbation may be applied before or after treating the mixed-mode coupling. In Li et al. (2024), rotational perturbations are added to pure p and g mode frequencies prior to solving the mixed-mode equation (equation 3). In contrast, Liagre et al. (2025) first compute mixed-mode frequencies, after which rotational perturbations are added. This approach, adopted by Liagre et al. (2025) to globally fit the quadrupolar modes, is an extension of the framework introduced by Deheuvels et al. (2017), in which the authors used stellar evolutionary models to locally fit asymmetric rotational multiplets of a single radial order. Whereas, Liagre et al. (2025) derived asymptotic expressions to globally fit the oscillation spectrum, yielding global seismic parameters for quadrupolar modes, i.e., q_2, $\Delta\Pi_2$, $\epsilon_{g,2}$, $\delta\nu_{02}$.

This paper is organized as follows. Section 2 describes the asymptotic theoretical model used to fit the oscillation spectrum of KIC 7341231. Section 3 discusses the Markov Chain Monte Carlo (MCMC) method employed to fit the oscillation spectrum, and the details of the grid-based stellar modeling used to determine the structure, composition, and age of KIC 7341231. Section 4 presents our results for the estimated seismic and structural parameters. Section 5 discusses the results and, finally, Section 6 summarizes the main conclusions of this work.

2. THEORETICAL MODEL

The power spectrum of the oscillating photometric signal of a star may be modeled as a sum of Lorentzian peaks centered around the resonant mode frequencies. Each mode eigenfunction is uniquely identified by three quantum numbers, the radial order n, and the harmonic degree ℓ and azimuthal order m of the spherical harmonic function Y_ℓ^m, which describes the spatial variation along the polar and azimuthal directions. With the resolution limitations of current telescopes, only disk-integrated photometry is possible for distant stars. Thus geometric-cancellation effects cause modes with harmonic degrees $\ell \geq 3$ to possess very low visibility. Although the $\ell = 3$ modes have visibility $\lesssim 10\%$ than that of the $\ell = 0$ modes, they are difficult to distinguish from the $\ell = 1$ and $\ell = 2$ mixed modes. Hence, in this work, we do not analyze modes with $\ell \geq 3$.

2.1. *p*, *g* and mixed-mode frequencies

In solar-like stars, gravity modes (g modes) are trapped in convectively stable layers (radiative zones), whereas pressure modes (p modes) propagate throughout the interiors. During the main-sequence phase, the p- and the g-mode frequencies remain far apart, and are dynamically uncoupled. As stars evolve, their radiative cores contract and convective envelopes expand, causing the g- and p-mode frequencies to approach each other, resulting in stronger coupling and therefore mixed modes. Indeed, asteroseismic observations of red giants and subgiants show significant coupling between the p and g modes (Bedding et al. 2010; Beck et al. 2011). Mixed modes have characteristics of both p and g modes (Chaplin & Miglio 2013; Unno et al. 1989) and may be used to infer deep-interior structure and dynamics.

For a spherically symmetric star with oscillations in the asymptotic regime, i.e., $n \gg \ell$, the second-order expression for p-mode frequencies is (Mosser et al. 2011):

$$\frac{\nu_{p:n_p,\ell}}{\Delta\nu} = \left(n_p + \frac{\ell}{2} + \epsilon_p\right) + \frac{\alpha}{2}\left(n_p - n_{\max}\right)^2 - d_{0\ell} + \beta_{0\ell}\left(n_p - n_{\max}\right), \tag{1}$$

where $\Delta\nu$ is the mean frequency spacing between successive radial modes ($\ell = 0$), ϵ_p an offset parameter, $d_{0\ell} \times \Delta\nu = \delta\nu_{02}$ the small frequency separation (García & Ballot 2019), and α accounts for the variation of $\Delta\nu$ with radial order n_p. Here, $n_{\max} = \nu_{\max}/\Delta\nu - \epsilon_p$, i.e., the radial order corresponding to a radial mode at $\nu_{\max}$ (the frequency at maximum power in the oscillation spectrum). The parameter $\beta_{0\ell}$ accounts for the variation of $d_{0\ell}$ with frequency (Lund et al. 2017; Liagre et al. 2025).

The asymptotic relation for g-mode frequencies is given by Mosser et al. (2012)

$$\frac{1}{\nu_{g:n_g,\ell}} = (-n_g + \epsilon_{g,\ell})\Delta\Pi_\ell, \tag{2}$$

where $\Delta\Pi_\ell$ is the period spacing between successive g modes, $n_g < 0$ is the radial order of the g mode, and $\epsilon_{g,\ell}$ is the offset parameter.

Mixed-mode frequencies are described by the following transcendental equation (Mosser et al. 2012):

$$\tan\theta_p = q_\ell \tan\theta_g, \tag{3}$$

where q_ℓ is the coupling factor, and θ_g and θ_p are the phases of the oscillatory eigenfunction at the inner and outer boundaries of the evanescent region, respectively, and are given by

$$\begin{aligned}\theta_p &= \pi\frac{\nu - \nu_p,}{\Delta\nu}, \\ \theta_g &= \frac{\pi}{\Delta\Pi_\ell}\left(\frac{1}{\nu} - \frac{1}{\nu_g}\right).\end{aligned} \tag{4}$$

Radial g modes do not exist, and the coupling between p and g modes for $\ell > 1$ is very weak (Unno et al. 1989). For the star analyzed in this work, $q_2 \sim 0.1q_1$.

2.2. Relative heights and widths

The observed amplitude of an oscillation mode is given by (García & Ballot 2019):

$$a_{n,\ell,m} = r_{\ell,m}(\iota)V_\ell A_n, \tag{5}$$

where A_n is the amplitude at the surface of the star, such that the observed fluctuation on the surface is $f_{n,\ell,m}(\theta,\phi) = A_n Y_\ell^m(\theta,\phi)$, where Y_ℓ^m is the spherical harmonic function. A_n varies with frequency (radial order), which we observe as the Gaussian-like profile of the p-mode envelope. V_ℓ is the mode visibility and $r_{\ell,m}$ denotes the relative amplitudes of modes of various m in a multiplet. $r_{\ell,m}$ depends on the inclination angle ι, which is the angle between the axis of rotation and the line of sight.

V_ℓ depends on the limb-darkening function and the measurement technique (García & Ballot 2019). V_ℓ is very low for $\ell > 2$, and therefore, only $\ell = 0 - 2$ modes are clearly visible in stellar oscillation power spectra. The $\ell = 3$ modes, if visible, possess very low amplitude. Visibility for $\ell = 1$ is higher than that of the $\ell = 0$ modes. By definition, $V_0^2 = 1$, and studies of various red giants have shown that, relative to V_0^2, $V_1^2 \in [1.2, 1.75]$, $V_2^2 \in [0.2, 0.8]$ and $V_3^2 \in [0, 0.1]$ (Mosser et al. 2012b).

The relative heights of different m components in a multiplet are given by

$$r^2_{\ell,m}(\iota) = \frac{(\ell - |m|)!}{(\ell + |m|)!}\left[P_\ell^{|m|}(\cos\iota)\right]^2, \tag{6}$$

where $P_\ell^{|m|}$ is the associated Legendre function.

Oscillations in solar-type stars are stochastically excited by turbulent convection near the stellar surface. For main-sequence stars, the heights and linewidths of the modes as a function of frequency are described by approximate empirical relations (Appourchaux, T. et al.

2014). In order to improve the precision of the estimates of heights and linewidths of the red giants we study, we treated the heights and linewidths of all radial modes as free parameters in the global fitting.

In this work, we fitted the spectrum of KIC 7341231 in the range from $\nu_{\max} - 3\Delta\nu$ to $\nu_{\max} + 3\Delta\nu$. The frequencies and heights of all the radial modes within this range were set as free parameters in the MCMC fit(see Section 3).

Based on energy-equipartition arguments and equation 5, the observed heights of the $\ell = 1$ and $\ell = 2$ pure p modes are given by V_2^1 and V_2^2 times the heights of $\ell = 0$ modes, respectively, and the linewidths are the same for all three. However, coupling between p and g modes induces mixed modes. For mixed modes, the linewidths are modeled as (Benomar et al. 2014)

$$\Gamma_\ell = (1 - \zeta_\ell)\,\Gamma_0, \tag{7}$$

where ζ_ℓ is the ratio of mode inertia in the g-mode cavity to the total mode inertia. All three, Γ_ℓ, Γ_0 and ζ_ℓ, are functions of ν.

An approximate expression for $\zeta(\nu)$ has been given by Deheuvels, S. et al. (2015),

$$\zeta(\nu) \simeq \left[1 + \frac{\nu^2 \Delta\Pi}{q\Delta\nu} \frac{\cos^2 \pi \dfrac{1}{\Delta\Pi}\left(\dfrac{1}{\nu} - \dfrac{1}{\nu_g}\right)}{\cos^2 \pi \dfrac{\nu - \nu_p}{\Delta\nu}}\right]^{-1}, \tag{8}$$

where $\zeta(\nu)$ ranges from 0 to 1. $\zeta(\nu) = 1$ for a pure g mode, and $\zeta(\nu) = 0$ for a pure p mode.

In order to model the heights of mixed modes, we used expressions from Mosser et al. (2018): for resolved modes, i.e., $\Gamma_\ell \geq 2\delta f_{\rm res}/\pi$ (where $\delta f_{\rm res}$ is the frequency resolution of the spectrum),

$$H_\ell = V_\ell^2 H_0, \tag{9}$$

and for unresolved modes, i.e., $\Gamma_\ell < 2\delta f_{\rm res}/\pi$,

$$H_\ell = V_\ell^2 . \frac{\pi}{2} \frac{\Gamma_\ell}{\delta f_{\rm res}} H_0. \tag{10}$$

2.3. Background noise model

The photometric signal also contains background noise, which may be modeled as the sum of Harvey profiles (Harvey 1985) and a frequency-independent white-noise term. At high frequencies, white noise dominates the signal, but at lower frequencies, granulation noise due to convection and stellar activity, and colored instrumental noise are more significant. Here, we use a modified form formulated by Kallinger, T. et al. (2014), which has been shown to provide the best background fits for main-sequence stars, sub-giants and red-giants, compared to older background models (Kallinger, T. et al. 2014; Corsaro, E. et al. 2020). The background model given by Kallinger, T. et al. (2014) is

$$B(\nu) = N_0 + \frac{a_1/b_1}{1 + (\nu/b_1)^2} + \eta^2(\nu)\left(\frac{a_2/b_2}{1 + (\nu/b_2)^4} + \frac{a_3/b_3}{1 + (\nu/b_3)^4}\right), \tag{11}$$

where a_i is the rms amplitude of the ith Harvey profile, and $b_i = (2\pi\tau_i)^{-1}$, where τ_i is the characteristic timescale. The factor $\eta(\nu)$ corresponds to the damping caused by discretized sampling (Kallinger, T. et al. 2014) and is given by $\eta = \mathrm{sinc}(\pi\nu/2\nu_{\rm nq})$, where $\nu_{\rm nq}$ is the Nyquist frequency. The parameter N_0 and the first Harvey profile account for instrumental noise: the former represents the constant white noise, while the latter represents frequency-dependent colored noise. Neither of these components is affected by the discretized sampling and are therefore not multiplied by $\eta^2(\nu)$.

2.4. Rotational splitting

In a hypothetical non-rotating spherically symmetric star, modes of different m are degenerate. Rotation and other deviations (such as magnetic field) break spherical symmetry, causing every multiplet with non-trivial harmonic degree $\ell > 0$ to split into $2\ell + 1$ component peaks ($m \in [-\ell, \ell]$) (García & Ballot 2019). For the constant, slow-rotation case, the rotational splittings are symmetric (ignoring higher-order effects of rotation, which are negligible in slowly rotating stars).

Applying perturbation theory, for slowly rotating stars, i.e., $\Omega << \nu_{n,l}$, the frequency of each m component may be written as:

$$\nu_{n,\ell,m} = \nu_{n,\ell} + \delta\nu_{n,\ell,m} + O(\Omega^2), \tag{12}$$

where $\delta\nu_{n,\ell,m}$ accounts for linear effects of rotation, and $O(\Omega^2)$ captures higher-order effects.

The first-order perturbation term $\delta\nu_{n,\ell,m}$ is given by (Deheuvels et al. 2017):

$$\delta\nu_{n,\ell,m} = \frac{m}{2\pi} \int_0^{R_\star} K_{n,\ell}(r)\Omega(r)dr, \tag{13}$$

where $K_{n,\ell}(r)$ is the rotation kernel, which defines the sensitivity of the (n, ℓ, m) eigenmode to rotation, and $\Omega(r)$ is the rotation profile of the star.

For a mixed mode, this equation can be modified as:

$$\delta\nu_{n,\ell,m} = \frac{m}{2\pi}\left[\int_{\rm core}\Omega(r)K_{n,\ell}(r)dr+\int_{\rm env}\Omega(r)K_{n,\ell}(r)dr\right], \tag{14}$$

where $K_{n,\ell}(r)$ is the sensitivity kernel for the mixed mode.

Defining $\beta_{n,\ell} = \int_0^{R_\star} K_{n,\ell}(r)dr$, and similarly $\beta_{n,\ell,\rm core} = \int_{\rm core} K_{n,\ell}(r)dr$ and $\beta_{n,\ell,\rm env} = \int_{\rm env} K_{n,\ell}(r)dr$, we can rewrite Equation 14 as

$$\delta\nu_{n,\ell,m} = \frac{m}{2\pi}\Big[\beta_{n,\ell,\rm core}\langle\Omega\rangle_{n,\ell,\rm core} + \beta_{n,\ell,\rm env}\langle\Omega\rangle_{n,\ell,\rm env}\Big], \tag{15}$$

where $\langle\Omega\rangle_{n,\ell,\rm core}$ and $\langle\Omega\rangle_{n,\ell,\rm env}$ are the weighted averages of the rotation rates over the core and the envelope, respectively, as defined below:

$$\begin{aligned}\langle\Omega\rangle_{n,\ell,\rm core} &= \frac{\int_{\rm core}\Omega(r)\,K_{n,\ell}(r)\,dr}{\int_{\rm core}K_{n,\ell}(r)\,dr},\\ \langle\Omega\rangle_{n,\ell,\rm env} &= \frac{\int_{\rm env}\Omega(r)\,K_{n,\ell}(r)\,dr}{\int_{\rm env}K_{n,\ell}(r)\,dr}.\end{aligned} \tag{16}$$

What we measure in the global fit are $\langle\Omega\rangle_{n,\ell,\rm core}$ and $\langle\Omega\rangle_{n,\ell,\rm env}$ averaged over all the radial orders, because these vary very slowly with n, for $n >> \ell$. For the sake of notional brevity, we omit the label n from the kernel-averaged rotation rates in the subsequent discussion. In contrast, $\beta_{n,\ell,\rm core}$ and $\beta_{n,\ell,\rm env}$ vary substantially with n, and under the asymptotic approximation, these may be written in terms of $\zeta_{n,\ell}$ (Goupil et al. 2013; Hasan, S. S. et al. 2005),

$$\begin{aligned}\beta_{n,\ell,\rm core} &\approx \left(1-\frac{1}{\ell(\ell+1)}\right)\zeta_{n,\ell}\ ,\\ \beta_{n,\ell,\rm env} &\approx 1-\zeta_{n,\ell}.\end{aligned} \tag{17}$$

Using this, we rewrite equation 15 as:

$$\begin{aligned}\delta\nu_{n,\ell,m} =& \frac{m}{2\pi}\Bigg[\left(1-\frac{1}{\ell(\ell+1)}\right)\zeta_{n,\ell}\,\langle\Omega\rangle_{\ell,\rm core}\\ &+(1-\zeta_{n,\ell})\langle\Omega\rangle_{\ell,\rm env}\Bigg].\end{aligned} \tag{18}$$

Equation 18 gives symmetric rotational splittings. This is valid when NDE are negligible. However, when the frequency separation between successive mixed modes is comparable to or smaller than the rotational splittings, NDE result in asymmetric multiplets as discussed in Section 1. Therefore, this expression cannot be used for $\ell = 2$ mixed modes, and the correct approach for fitting quadrupolar mixed modes is described below.

2.5. Near-degeneracy effects on rotational splittings of $\ell = 2$ modes

As mentioned in Section 1, we use the approach from Li et al. (2024) to fit the asymmetric rotational splittings in $\ell = 2$ modes. First, we add the rotation perturbation term from equation 18 to the asymptotic pure p- and g-mode frequencies, i.e.:

$$\begin{aligned}\nu_{p;n_p,\ell,m} &= \nu_{p;n_p,\ell} - \frac{m}{2\pi}\langle\Omega\rangle_{\ell,\rm env}\ ,\\ \nu_{g;n_g,\ell,m} &= \nu_{g;n_g,\ell} - \frac{m}{2\pi}\left(1-\frac{1}{\ell(\ell+1)}\right)\langle\Omega\rangle_{\ell,\rm core}\ ,\end{aligned} \tag{19}$$

where $\nu_{p;n_p,l}$ and $\nu_{g;n_g,l}$ are given by equations 1 and 2. For pure p and g modes, $\zeta_{n,\ell} = 0$ and 1, respectively, in equation 18.

After adding the rotation terms with $\langle\Omega\rangle_{\ell,\rm env}$ and $\langle\Omega\rangle_{\ell,\rm core}$, which are free parameters in the asymptotic fit for $\ell = 2$ modes, separate mixed-mode equations (equation 3) are solved for each m, i.e.,

$$\tan\theta_{p,m} = q_\ell \tan\theta_{g,m}. \tag{20}$$

NDE are much smaller for dipolar modes. This is due to the stronger coupling between p and g-mode cavities, which results in much larger spacings between successive mixed modes than the rotational splittings. However, NDE also begin to appear in dipolar modes as red giants evolve, especially beyond $\Delta\nu \gtrsim 14\,\mu$Hz (Li et al. (2024)), because the coupling strength decreases while the core rotation rate increases.

2.6. Latitudinal differential rotation

In the absence of latitudinal differential rotation, $\langle\Omega\rangle_{2,\rm env}$ and $\langle\Omega\rangle_{2,\rm core}$ in equation 19 are independent of m. However, due to latitudinal differential rotation, these are different for $m = \pm1$ and $m = \pm2$ modes, as the Kernel functions $K_{2,\pm1}(r,\theta)$ and $K_{2,\pm2}(r,\theta)$ are different (Gizon & Solanki 2004; Benomar et al. 2018). Hence, the splitting between $m = 0$ and $m = \pm1$ quadrupolar modes is not the same as the splitting between $m = \pm1$ and $m = \pm2$ modes.

In this work, we assume negligible differential rotation in the core, as has been observed in the Sun. Thus,

$\langle\Omega\rangle_{2,\text{core}}$ is independent of m. Moreover, in the asymptotic regime, $\langle\Omega\rangle_{2,\text{core}} \simeq \langle\Omega\rangle_{1,\text{core}}$. Therefore, in the MCMC fit for quadrupolar modes, we use the same core rotation value obtained from the $\ell = 0, 1$ fit and keep it fixed. Whereas, to test the possibility of measurable differential rotation in the envelope, we perform two fits for $\ell = 2$ modes: one with fixed $\langle\Omega\rangle_{2,\text{env}}$ and another with free $\langle\Omega\rangle_{2,\text{env}}$. If this second fit and the $\ell = 0, 1$ fit yield values of the envelope rotation consistent to within error bars, this implies that the differential rotation is smaller than the measurable limit. Otherwise, the m-dependence of $\langle\Omega\rangle_{2,\text{env}}$ should be accounted for in equation 19. For KIC 7341231, we found consistent envelope rotation rates from the $\ell = 2$ and $\ell = 0, 1$ fits.

3. METHODS

The oscillation spectrum of KIC 7341231 was fitted to the theoretical model described above using the Markov Chain Monte Carlo (MCMC) method. It is a young red giant with $\Delta\nu = 29\,\mu$Hz and $\Delta\Pi = 111\,$s (see Table 4). The fitting was performed in two steps– First, the $\ell = 0$ and $\ell = 1$ modes were fitted using a modified version of the `TAMCMC-C` code, developed by O. Benomar (Benomar, O. et al. (2009)). After obtaining the best-fit parameters from this step, the $\ell = 2$ modes were fitted using a different MCMC code, written in Python using the `emcee` package. For this second fit, all the parameters related to the $\ell = 0$ and $\ell = 1$ modes were kept fixed.

3.1. **Data**

We used Kepler's short-cadence photometric data. There is a long gap in the data from one-third of quarter Q1 to the end of quarter Q4. We therefore used data from Q5 to Q17 (3.14 years), which is nearly continuous with a 91% duty cycle. We downloaded the PDCSAP light curves, produced by the Kepler Science Operations Center (SOC) pipeline, from the MAST (Mikulski Archive for Space Telescopes) archive. We used the `lightkurve` package in Python to download the data. We did not fill the gaps in the data. The power spectrum was computed using 'lightkurve.to_periodogram( )' function, after removing the outliers with the 'lightkurve.remove_outliers()' function.

3.2. **Markov Chain Monte Carlo**

Markov Chain Monte Carlo (MCMC) sampling is a standard method applied to fit stellar oscillation power spectra. It is preferred over other standard methods, because it overcomes the problem of convergence to local maxima and also provides reliable uncertainties, even when the posteriors are multi-modal.

Using Bayes' theorem, the posterior probability density function is given by

$$\pi(\boldsymbol{\theta} \mid \boldsymbol{y}, M) \propto \pi(\boldsymbol{\theta} \mid M)\pi(\boldsymbol{y} \mid \boldsymbol{\theta}, M), \tag{21}$$

where $\pi(\boldsymbol{\theta} \mid M)$ is the prior probability, set using the prior knowledge of the fit parameters, and $\pi(\boldsymbol{y} \mid \boldsymbol{\theta}, \mathrm{M})$ is the probability of observing data $\boldsymbol{y}$, given a theoretical model M with a set of parameters $\boldsymbol{\theta}$, which is also termed the Likelihood function.

The noise statistics for each data point y_i at frequency ν_i are independent and are described by a χ^2 distribution with 2 degrees of freedom. Hence, the likelihood is given by (Appourchaux, T. et al. (1998); Benomar, O. et al. (2009)):

$$\pi(\boldsymbol{y} \mid \boldsymbol{\theta}, M) = \prod_{i=1}^{N} \frac{1}{M(\nu_i, \boldsymbol{\theta})} \exp\left(-\frac{y_i}{M(\nu_i, \boldsymbol{\theta})}\right). \tag{22}$$

The oscillation signal also contains background noise, as discussed in Section 2.3. Therefore, the model $M(\nu_i, \boldsymbol{\theta})$ is given by the sum of the stellar oscillation model $S(\nu_i, \boldsymbol{\theta_S})$ and the background noise model $B(\nu_i, \boldsymbol{\theta_N})$

$$M(\nu_i, \boldsymbol{\theta}) = S(\nu_i, \boldsymbol{\theta_S}) + B(\nu_i, \boldsymbol{\theta_N}). \tag{23}$$

Here, $\boldsymbol{\theta_S}$ and $\boldsymbol{\theta_N}$ are subsets of $\boldsymbol{\theta}$, comprising the seismic and noise parameters, respectively.

The spectral model $S(\nu_i, \boldsymbol{\theta_S})$ is the sum of several Lorentzian profiles corresponding to the resonance peaks in the spectrum. Their heights $H_{n,\ell,m}$, center frequencies $\nu_{n,\ell,m}$, and linewidths $\Gamma_{n,\ell,m}$ are given by the asymptotic theory described in Section 2. Thus,

$$S(\nu_i, \boldsymbol{\theta_S}) = \sum_{\ell,m,n} \frac{H_{n,\ell,m}}{1 + \left(\frac{2(\nu - \nu_{n,\ell,m})}{\Gamma_{n,\ell,m}}\right)^2}. \tag{24}$$

3.2.1. *MCMC fitting of radial and dipolar modes*

The power spectrum was first fitted with the background model $B(\nu_i, \boldsymbol{\theta_N})$, given by Equation 11, using Gaussian Process Optimization (GPO) (Jones et al. 1998; Frazier 2018). The background noise parameters θ_N, obtained from this fit, are listed in Table 10 in the Appendix. These parameters were kept fixed while fitting the oscillation modes.

We used the same MCMC framework as in the latest version of O. Benomar's `TAMCMC-C` code, available at *https://github.com/OthmanB/TAMCMC-C*. However, we modified the theoretical model wherever required. We adopted the theoretical model described in Section 2.

`TAMCMC-C` uses the Metropolis-Hastings algorithm (Metropolis et al. (1953); Hastings (1970)) with multiple parallel chains to sample the parameter space. We used 8 parallel chains in our analysis. The temperatures of the chains follow a geometric sequence, $T = \lambda^{n-1}$, with λ fixed to a value such that the maximum temperature is close to 100. We sample 400k samples in the burn-in phase, 700k samples in the learning phase, and 500k samples in the acquisition phase. We use the last 400k of the acquisition phase to construct the posterior distributions. In the learning phase, `TAMCMC-C` uses an adaptive MCMC algorithm, based on Atchadé (2006), to optimize the acceptance rate. The adaptive algorithm constantly adjusts the covariance matrix of the Gaussian proposal distribution (see Benomar, O. et al. (2009) for details). With this method, we achieve an acceptance rate greater than 0.20.

To assess convergence of the MCMC posteriors, we divide the 400k samples into two halves, and compare the resulting posteriors for medians and $\pm 1\sigma$ confidence intervals. For multi-modal posteriors, we also examine the number of modes, peak locations, and relative heights. If the two sets of posteriors are in statistical agreement, this implies that the sampling has converged to the target distributions. Furthermore, we repeat the MCMC runs (at least once) to verify the consistency of the best fits.

3.2.2. *Priors for the $\ell = 0, 1$ fit*

The parameter space $\boldsymbol{\theta}$ comprised 27 parameters in total– 18 for frequencies, heights, and linewidths of the six radial modes, 6 parameters for the $\ell = 1$ mixed modes: $\Delta\Pi_1$, q_1, $\epsilon_{g,1}$, d_{01}, β_{01}, and visibility V_1^2, 2 parameters for the rotation rates, $\langle\Omega\rangle_{1,\mathrm{core}}$ and $\langle\Omega\rangle_{1,\mathrm{env}}$, and the last one for the inclination. The fitting parameters are listed in Table 1, along with the priors adopted for each. $\Delta\nu$, ϵ_p, and α are computed internally by fitting the sampled $\ell = 0$ frequencies with equation 1.

Default Jeffreys priors were used for the heights and linewidths of the radial modes, while Gaussian–Uniform–Gaussian (GUG) priors were used for the frequencies. A GUG prior consists of a uniform distribution with Gaussian edges on the sides. The half-widths of the Gaussian edges were set to 0.25% of $\Delta\nu$. For Jeffreys priors, the default lower and upper bounds were adopted (see Table 1). For the frequencies, the bounds of the uniform window in the GUG priors were set to $\pm 0.5\,\mu$Hz around the initial guesses.

The initial guesses for the frequencies, heights, and linewidths of the $\ell = 0$ modes were obtained by pre-fitting them locally with Lorentzian functions, using Maximum Likelihood Estimation (MLE) - implemented by calling the 'minimize' function of the `scipy.optimize` module. An estimate of $\Delta\nu$ was also computed from the initial guesses of the radial-mode frequencies. This estimate was then used in defining the priors for other parameters (see Table 1).

Uniform priors were used for all mixed-mode parameters, as well as for the rotation rates and inclination. The corresponding prior ranges are listed in Table 1. Since parallel tempering is implemented in the `TAMCMC-C` code, the final converged fits are independent of the initial guess values. The linewidths and heights of the mixed modes were computed using equations 7 to 10.

3.2.3. *MCMC fitting of quadrupolar modes*

After obtaining the seismic parameters from the $\ell = 0, 1$ fit, the spectrum was fitted for the $\ell = 2$ modes using another MCMC code written in Python, employing the `emcee` package. For this fit, the parameters related to $\ell = 0$ and $\ell = 1$ modes were kept fixed.

The `emcee` sampler is based on the Goodman & Weare MCMC algorithm (Goodman & Weare (2010)). It is an affine-invariant ensemble sampler that uses a group of walkers, which propose moves based on the positions of other walkers in the ensemble. Affine-invariance implies that the sampler performance is unaffected by linear stretching, rotation, or rescaling of the parameter space. The Metropolis–Hastings algorithm used in traditional MCMC methods needs careful tuning of the proposal covariance matrix, whereas this sampler provides robust posterior sampling with minimal tuning (see Goodman & Weare (2010) for details). We did not incorporate parallel tempering in this MCMC code.

3.2.4. *Priors for the $\ell = 2$ fit*

As explained in Section 2.6, we performed two fits for the $\ell = 2$ modes: one in which both the core and envelope rotation rates, $\langle\Omega\rangle_{2,\mathrm{core}}$ and $\langle\Omega\rangle_{2,\mathrm{env}}$, were fixed to the values obtained from the $\ell = 0, 1$ fit, and another in which $\langle\Omega\rangle_{2,\mathrm{env}}$ was free. The other free parameters for the $\ell = 2$ fits are – $\Delta\Pi_2$, q_2, $\epsilon_{g,2}$, d_{02}, β_{02}, V_2^2. All parameters related to the $\ell = 0$ and $\ell = 1$ modes were kept fixed to the best-fit values obtained from the $\ell = 0, 1$ fit.

Uniform priors were set for all free parameters, and the prior ranges are given in Table 2.

Table 1: List of all fitting parameters for the $\ell = 0, 1$ MCMC fit, along with the types of prior distributions and the adopted prior ranges. GUG: Gaussian-Uniform-Gaussian.

Parameter	**Prior type**	**Prior range**
$\ell = 0$ frequencies (6 radial orders)	GUG	Uniform window of $\pm 0.5\,\mu$Hz around the initial guesses obtained from local fits; Default half-width for the Gaussian edges (0.25% of $\Delta\nu$)
Heights of $\ell = 0$ modes	Jeffreys	Initial guesses obtained from local fits; Default bounds $[H_{\rm min} = 1,\ H_{\rm max} = 400000]$
Linewidths of $\ell = 0$ modes	Jeffreys	Initial guesses obtained from local fits; Default bounds $[\Gamma_{\rm min} =$ frequency resolution, $\Gamma_{\rm max} = \Delta\nu/3]$
d_{01}	Uniform	-10 to 10% of $\Delta\nu$
$\Delta\Pi_1$	Uniform	95 to 120 s
q_1	Uniform	0.1 to 0.6
$\epsilon_{g,1}$	Uniform	0 to 1
β_{01}	Uniform	0.00 to 0.05
Visibility of $\ell = 1$ modes	Uniform	0.5 to 2.0
$\langle\Omega\rangle_{1,\rm core}/2\pi$	Uniform	100 to 2000 nHz
$\langle\Omega\rangle_{1,\rm env}/2\pi$	Uniform	0 to 300 nHz
Inclination angle	Uniform	0 to 90°

Table 2: List of all fitting parameters for the $\ell = 2$ MCMC fit, along with the types of prior distributions and the adopted prior ranges.

Parameter	**Prior type**	**Prior range**
d_{02}	Uniform	-15 to -9% of $\Delta\nu$
$\Delta\Pi_2$	Uniform	$\Delta\Pi_1/\sqrt{3} \pm 2.0$ s
q_2	Uniform	0.02 to 0.06
$\epsilon_{g,2}$	Uniform	0 to 1
β_{02}	Uniform	0.00 to 0.05
Visibility of $\ell = 2$ modes	Uniform	0.1 to 1.0
$\langle\Omega\rangle_{2,\rm env}/2\pi$	Uniform	0 to 150 nHz

From asymptotic theory,

$$\Delta\Pi_l = \frac{\Delta\Pi_0}{\sqrt{\ell(\ell+1)}}, \tag{25}$$

where

$$\Delta\Pi_0 = 2\pi^2 \left(\int_{g-\rm cavity} \frac{N}{r} dr \right), \tag{26}$$

and N is the Brunt–Väisälä frequency. Using this, we set a tight prior for $\Delta\Pi_2$, centred around $\Delta\Pi_1/\sqrt{3}$.

The initial guesses for q_2 and d_{02} are obtained by locally fitting one of the radial orders that has previously been analysed in Deheuvels et al. (2017), using stellar models. We constrained the fit to best match the unperturbed $m = 0$ quadrupolar frequencies reported in Deheuvels et al. (2017). This yielded $q_2 \approx 0.04$ and $d_{02} \approx 11.7\%$ of $\Delta\nu$. We set uniform priors of approximately $\pm 50\%$ and $\pm 25\%$ around these values, respectively. For $\epsilon_{g,2}$ we allowed all values from 0 to 1, and for β_{02}, a uniform prior similar to that of β_{01} was used. We allowed Visibility V_2^2, to vary from 0.1 to 1.0. For $\langle\Omega\rangle_{2,\rm env}$, we used a very broad prior range around the best-fit $\langle\Omega\rangle_{1,\rm env}$, obtained from the $\ell = 0, 1$ fit.

3.3. Stellar models

3.3.1. *Input physics and parameter ranges*

We generated stellar models using the open-source stellar evolution code MESA (Paxton et al. (2010); Paxton et al. (2011, 2013, 2015, 2018, 2019)). We adopted the same input physics as in Li et al. (2022), including opacities, equation of state, atmospheric model, convective overshooting, atomic diffusion and the mass-loss prescription. The only difference is that we used the Canuto-Goldman-Mazzitelli (CGM) convection model (Canuto et al. (1996)) in place of the standard mixing-length theory. This choice allows us to compare our results with those of Deheuvels, S. et al. (2012).

The ranges for the stellar mass, helium mass fraction $Y_{\rm in}$ and metal mass fraction $Z_{\rm in}$ (see Table 3), were chosen to at least encompass those used in Deheuvels, S. et al. (2012) for the same star. In that work, the metallicity range is -1.75 to -0.75 and $Y_{\rm in}$ is constrained by the Helium enrichment law: $Y = Y_p + (\Delta Y/\Delta Z)\cdot Z$ with $\Delta Y/\Delta Z = 3 \pm 2$ (Pagel & Portinari (1998); Peimbert et al. (2007)). This corresponds to 0.248 to 0.260 for $Y_{\rm in}$ and 0.00024 to 0.0024 for $Z_{\rm in}$. For a metal-poor star such as KIC 7341231 (see Table 6 for the observed surface metallicity), values of $Y_{\rm in}$ above 0.26 are significantly higher than those predicted by the helium enrichment law, and would imply either a helium-enhanced formation history or other non-standard evolutionary scenarios. However, we did not impose the helium enrichment law constraint in this study and instead used a broader range for $Y_{\rm in}$, similar to the range used in Li et al. (2022) for modeling red giants. Moreover, we also show in Section 4 how the stellar parameter inferences change when the helium enrichment law constraint is applied.

We implemented the CGM model in MESA following an earlier implementation by Warrick Ball for an older version of the code, available in the MESA users mailing list archive. Our modified MESA source code with the CGM implementation is available on GitHub.

In the CGM framework, the characteristic scale of the largest energy-carrying turbulent eddies is often modeled as $l = \alpha_{\rm CGM} H_p$, where H_p is the pressure scale height and $\alpha_{\rm CGM}$ is treated as a free parameter in stellar modeling. Solar-calibrated values of $\alpha_{\rm CGM}$ reported in the literature lie in the range 0.6–0.8 (Samadi, R. et al. (2006); Piau, L. et al. (2011); Sonoi, T. et al. (2019)). These values vary depending on the adopted stellar evolution code, physical modeling, solar metallicity, etc. To our knowledge, no published study addresses the implementation of the CGM model in MESA. We therefore performed a solar calibration, with the same input physics as adopted for KIC 7341231, and obtained $\alpha_{\rm CGM} = 0.90$. For KIC 7341231, we did not fix $\alpha_{\rm CGM}$ to this solar-calibrated value; instead, we treated it as a free parameter in the GPO exploration, with an allowed range of 0.6 to 1.5.

Table 3: Parameter ranges used for the Gaussian Process Optimization (GPO). Each evolutionary track was evolved until it reached the observed value of $\Delta\nu$. The `time_delta_coefficient` parameter in the MESA source code was set to obtain a temporal resolution of approximately 0.5 Myr in the vicinity of the target $\Delta\nu$.

Parameter	**Range**
Mass ($M_\odot$)	0.70 – 1.0
$Z_{\rm in}$	0.0001 – 0.003
$Y_{\rm in}$	0.24 – 0.30
$\alpha_{\rm CGM}$	0.6 – 1.5

3.3.2. *Oscillation frequencies*

Each evolutionary track was evolved until its $\Delta\nu$ (computed by MESA using the scaling relation) matches the observed value. The time step was also reduced to $\sim$ 0.5 Myr in the vicinity of the target $\Delta\nu$. For each evolutionary track, only the models within the range $\Delta\nu_{\rm obs} + 3\,\mu$Hz to $\Delta\nu_{\rm obs}$ were retained. The oscillation frequencies for these models were computed using GYRE (Townsend & Teitler (2013)). The $\Delta\nu$ values computed internally by MESA using scaling relation were typically 1–2 μHz higher than those obtained by fitting the GYRE frequencies. Therefore, GYRE was run for all the models within the $\Delta\nu_{\rm obs} + 3\,\mu$Hz to $\Delta\nu_{\rm obs}$ range.

3.3.3. *Surface corrections*

To correct for surface effects arising from imperfect modeling of the stellar surface, we used the surface correction formalism from Ball & Gizon (2014). For each model, the correction coefficients were fit using the radial and dipolar modes. After this, the corresponding corrections were added to all modes, including $\ell = 0, 1$ and 2. The $\ell = 2$ mixed modes were excluded from the fitting process to avoid overfitting. The surface corrections for the mixed modes were scaled by a factor of $1/Q$ where Q is the ratio of the mixed-mode inertia to the inertia of a radial mode interpolated to the same frequency (Aerts et al. (2010); Deheuvels, S. et al. (2012)). We included four additional radial modes from outside the frequency range used for the asymptotic fit ($\nu_{\rm max} - 3\Delta\nu$ to $\nu_{\rm max} + 3\Delta\nu$), to improve the estimation of the surface correction. We did not extend the range of the asymptotic fit, as doing so degraded the fit of the $\ell = 1$ and $\ell = 2$ mixed-mode frequencies.

For the Sun, at higher order frequencies, the contribution from the inverse term (with coefficient a_{-1}) is typically an order of magnitude smaller than that from the cubic term (with coefficient a_3) (Ball, W. H. & Gizon, L. 2017). The lowest radial-mode frequency used in our analysis of KIC 7341231 is at 271.15 μHz, which is approximately $\nu_{\rm max} - 5\Delta\nu$. In the Sun, for an oscillation mode near $\nu_{\rm max} - 5\Delta\nu$, the contribution from the inverse term is approximately 10% of the cubic term contribution in calibrated solar models, and the total surface correction is about 1 μHz (Ball, W. H. & Gizon, L. (2017)). However, this ratio could be larger in evolved solar-like stars. (Ball et al. (2018)). We therefore did not ignore the inverse term completely. Instead, we first performed our analysis using only the cubic term, and then repeated it using both the cubic and inverse terms. To avoid overfitting when applying the combined correction, we rejected models for which the contribution of the inverse term to the lowest radial mode (at 271.15 μHz) exceeded the cubic term contribution.

3.3.4. *Optimization method*

We employed a level-set Bayesian optimization framework with a Gaussian Process surrogate model to efficiently explore the parameter space for models that provide an acceptable fit to the observational constraints (Pramanik et al. in prep). This technique uses a Gaussian Process as a surrogate model of an expensive objective function, to adaptively select new evaluation points that are most informative for identifying regions in parameter space consistent with the observational constraints. This enables efficient optimization with a limited number of costly function evaluations.

During the Bayesian optimization, before applying surface corrections, we rejected models with $|\Delta\nu_{\rm obs} - \Delta\nu_{\rm mod}| > 2\,\mu$Hz, as well as those for which any of the $\ell = 0$ frequencies were outside the range $\nu_{\rm obs} \pm 8\,\mu$Hz. The frequency bounds were kept wider to account for surface effects. Surface corrections in sub-giants and young red giants with $\nu_{\rm max} \sim 400$–$800\,\mu$Hz and masses $\sim 1 - 1.5{\rm M}_\odot$ are expected to be $< 5\,\mu$Hz (Ball, W. H. & Gizon, L. 2017).

To compute $\Delta\nu_{\rm mod}$ for each model, we fitted the radial-mode frequencies using Equation 1. This was preceded by a linear fit to the radial-mode frequencies to determine the radial order of the lowest $\ell = 0$ mode, thereby ensuring consistent matching of the radial orders (n_p) between the observed and model frequencies. In this preliminary fit, $\Delta\nu$ and ϵ_p were also treated as free parameters. However, the value of $\Delta\nu_{\rm mod}$ used to apply the filter was obtained from the subsequent quadratic fit.

4. RESULTS

4.1. **Best-fit spectrum model**

The best-fit model for the oscillation spectrum of KIC 7341231 is shown in Figure 1. The $\ell = 0$, $\ell = 1$ and $\ell = 2$ modes are plotted in black, blue and red, respectively, and the power spectrum is plotted in gray. Zoomed-in plots for three radial orders around $\nu_{\rm max}$ are shown in Figure 2. The $m = 0$, $m = \pm1$ and $m = \pm2$ quadrupolar mixed modes are marked with different colors.

To compute the best-fit model, the medians of the posteriors of all the free parameters in the $\ell = 0, 1$ and $\ell = 2$ fits (see Section 3) were inserted into the theoretical model described in Section 2. The median values of all global parameters, along with their upper and lower 1-sigma uncertainties, corresponding to 68% confidence intervals, are listed in Tables 4 and 5. For $\ell = 2$ modes, best-fit parameters are reported for the two cases: one with fixed envelope rotation and the other with free envelope rotation. Corner plots for all MCMC fits are shown in Figures 3, 4 and 5.

We obtained the same envelope rotation rate, within the error bars, from quadrupolar and dipolar mixed modes. However, for KIC 7341231, this agreement does not provide any information about latitudinal differential rotation because the $m = \pm1$ quadrupolar modes are not visible in the spectrum due to the high inclination angle(80°). Under the asymptotic approximation, $\langle\Omega\rangle_{2,\pm2,\rm env} \simeq \langle\Omega\rangle_{1,\pm1,\rm env}$ (Gizon & Solanki 2004; Benomar et al. 2018), whereas $\langle\Omega\rangle_{2,\pm1,\rm env}$ differs in the presence of latitudinal differential rotation. Therefore, both $m = \pm1$ and $m = \pm2$ quadrupolar modes are required to constrain latitudinal differential rotation.

Our best-fit values for all fitting parameters are in agreement with the values reported by Liagre et al. (2025), to within the error bars (see Table 1 in Liagre et al. 2025)). This shows that the approach we employed, following Li et al. (2024), is consistent with the method used in Liagre et al. (2025), at least for young red giants and subgiants. Therefore, both approaches can be reliably used for characterizing quadrupolar mixed modes in young red giants and subgiants.

4.2. **Importance of quadrupolar modes in constraining the structural model**

4.2.1. *Observational constraints*

We used the observed frequencies, along with the atmospheric observables $T_{\rm eff}$ and surface metallicity, to constrain the structural parameters of KIC 7341231. We used the locally fitted frequency measurements from De-

Table 4: Best-fit seismic parameters obtained from the $\ell = 0, 1$ MCMC fit. The given values are the medians of the MCMC posteriors of the fitting parameters, and the upper and lower errors correspond to $\pm 1\sigma$ confidence interval.

Parameter	Medians with 1-sigma errors
$\Delta\nu$	$29.005^{+0.004}_{-0.004}\,\mu$Hz
ϵ_p	$0.255^{+0.002}_{-0.002}$
α	$0.0078^{+0.0002}_{-0.0002}$
$d_{01} \times \Delta\nu$	$-0.08^{+0.02}_{-0.02}\,\mu$Hz
$\Delta\Pi_1$	$111.23^{+0.03}_{-0.02}$ s
q_1	$0.376^{+0.001}_{-0.001}$
$\epsilon_{g,1}$	$0.301^{+0.005}_{-0.005}$
β_{01}	$0.0061^{+0.0004}_{-0.0004}$
V_1^2	$1.13^{+0.06}_{-0.06}$
$\langle\Omega\rangle_{1,\rm core}/2\pi$	770^{+14}_{-14} nHz
$\langle\Omega\rangle_{1,\rm env}/2\pi$	51^{+15}_{-14} nHz
Inclination	80^{+2}_{-2} deg

Table 5: Best-fit seismic parameters obtained from the $\ell = 2$ MCMC fit.

Parameter	With fixed $\langle\Omega\rangle_{2,\rm core}$ and $\langle\Omega\rangle_{2,\rm env}$	With fixed $\langle\Omega\rangle_{2,\rm core}$ and free $\langle\Omega\rangle_{2,\rm env}$
$d_{02} \times \Delta\nu$	$3.40^{+0.02}_{-0.02}\,\mu$Hz	$3.41^{+0.02}_{-0.02}\,\mu$Hz
$\Delta\Pi_2$	$64.416^{+0.006}_{-0.006}$ s	$64.416^{+0.006}_{-0.005}$ s
q_2	$0.0382^{+0.0004}_{-0.0005}$	$0.0382^{+0.0004}_{-0.0004}$
$\epsilon_{g,2}$	$0.138^{+0.003}_{-0.004}$	$0.138^{+0.003}_{-0.004}$
β_{02}	$0.0085^{+0.0005}_{-0.0005}$	$0.0084^{+0.0005}_{-0.0005}$
V_2^2	$0.40^{+0.02}_{-0.02}$	$0.40^{+0.02}_{-0.02}$
$\langle\Omega\rangle_{2,\rm env}/2\pi$	–	40^{+5}_{-5} nHz

heuvels, S. et al. (2012). We did not use the frequency measurements obtained from the global asymptotic fit presented in this paper because the MCMC-derived uncertainties in the fitted frequencies are much smaller than the actual uncertainties. This is because global asymptotic fits assume that the asymptotic relations are exact, whereas stars exhibit departures from the ideal asymptotic pattern. The measured values of $T_{\rm eff}$ and [M/H] were also adopted from the same work (see Table 6). We did not use $\log g$ to constrain the structure, as was done in Deheuvels, S. et al. (2012), because it is a redundant constraint when computed using the scaling relation between $\log g$, $T_{\rm eff}$ and $\nu_{\rm max}$ (Brown et al. 1991).

We used all $\ell = 0$ frequencies from Table 2 of Deheuvels, S. et al. (2012); however for $\ell = 1$ and $\ell = 2$, we used only those frequencies that lie within the frequency range over which we fitted the oscillation spectrum using the asymptotic model (see Figure 1). This is because we needed the correct sequence of mixed modes from the asymptotic fit to correctly match the radial orders of the observed and model frequencies. This selection yielded a total of 32 frequencies: 10 $\ell = 0$, 16 $\ell = 1$, and 6 $\ell = 2$ frequencies.

We first explored the entire parameter space using our level-set Gaussian-Process Optimization (GPO) method to search for models with oscillation frequencies and atmospheric parameters close to the observed values. The method will be described in detail in Pramanik et al. in prep. To achieve adequate sampling of the full parameter space, we partitioned the mass dimension into 30 bins and performed an independent GPO optimization in each bin. During each exploration, the GPO generated 1400 evolutionary tracks and $\sim 50-60$ models for each track around the target $\Delta\nu$, with a temporal resolution of ~ 0.5 Myr.

Table 6: Atmospheric observables used to constrain the stellar structure. The adopted values are taken from Deheuvels, S. et al. (2012).

Observable	Adopted value
$T_{\rm eff}\,(K)$	5470 ± 150
[M/H] (dex)	-1.4 ± 0.1

$\Delta\nu$ and frequency filters were applied to all the models generated during the GPO exploration, as described in Section 3.3.4. The filtered models were then fitted for surface corrections (Section 3.3.3). After applying the surface corrections, then mean χ^2 was computed as:

$$\overline{\chi}^2 = \frac{1}{N}\sum_k \frac{(Y_{k,\rm obs} - Y_{k,\rm mod})^2}{\sigma^2_{Y_{k,\rm obs}}}, \tag{27}$$

where Y_k represents the observables used to constrain the stellar model, and N is the total number of observables.

Since there are 32 oscillation frequencies and two atmospheric observables, the seismic observables dominate the $\overline{\chi}^2$ and, hence, largely determine the best-fit model. Nevertheless, $T_{\rm eff}$ and [M/H] of the resulting best-fit models (see Table 7) are consistent with the measurements reported in previous studies, most of which are compiled in Table 1 of Deheuvels, S. et al. (2012). For $T_{\rm eff}$ and [M/H], the reported values range from 5233–6000 K and −2.18–−0.79 dex, respectively.

4.2.2. *Best-fit stellar model*

To assess how the stellar parameter inferences improve with the inclusion of quadrupolar modes, we computed $\overline{\chi}^2$ with and without the quadrupolar modes. The best-fit models obtained in the two cases are listed in Table 7, along with their corresponding $\overline{\chi}^2$ values. $\overline{\chi}^2_{A01}$ and $\overline{\chi}^2_{A012}$ denote the chi-square values computed without and with the quadrupolar modes, respectively. As discussed in Section 3.3.3, we performed the analysis with both the cubic and combined (cubic+inverse) surface corrections. Best-fit models obtained in both cases are listed in Table 7. The échelle diagrams for the corresponding best-fit models are shown in Figures 6 and 7, respectively. Model frequencies of the best-fit models are shown together with the observed frequencies from Deheuvels, S. et al. (2012) , which we used to constrain the stellar models, as well as the frequencies obtained from our MCMC fits based on the asymptotic model.

After including the quadrupolar modes in the χ^2 analysis, the best-fit mass, age, radius, initial helium fraction, and initial metallicity of KIC 7341231 changed by 0.2%, 1.7%, 0.4%, 1.6%, and 0.2%, respectively, for the case with the cubic surface correction. For the case with the combined surface correction, these parameters changed by 0.4%, 3.6%, 0.4%, 3.2%, and 0.3%, respectively.

The best values of $\overline{\chi}^2$ obtained with the cubic surface correction are 3.1 and 4.7 without and with the inclusion of $\ell = 2$ modes, respectively (see Table 7). These values, being greater than 1, reflect the systematic errors in the model frequencies due to limitations of theoretical models in accurately reproducing the true stellar structure. The $\overline{\chi}^2$ values with the combined correction are slightly better than with the cubic correction alone (see Table 7). However, the additional degree of freedom can overcorrect a model (Ball et al. (2018)). Assessing which surface-correction formalism is superior is beyond the scope of this paper.

4.2.3. *Assessing the constraining power of quadrupolar modes*

Determining precise $1-\sigma$ confidence intervals for stellar parameters is challenging when using individual frequencies as observational constraints (Li et al. 2023). This is because systematic modeling errors in the theoretical frequencies, arising from imperfections in the input physics, are comparable to, or even larger than, the statistical uncertainties in the observed frequencies (Li et al. 2022, 2023; Deheuvels, S. et al. 2014; Ball, W. H. & Gizon, L. 2017), and robustly quantifying these systematic uncertainties remains challenging (Li et al. 2023). When theoretical systematic errors are important, a likelihood based solely on the statistical uncertainties of the observed frequencies does not adequately represent the total uncertainty. Consequently, using only the statistical uncertainties in the χ^2 computation (Equation 27) leads to an over-constrained likelihood and, therefore, unrealistically small uncertainties in the inferred stellar parameters (Ball, W. H. & Gizon, L. 2017; Li et al. 2023). With interpolated grids, observational uncertainties can be propagated through repeated Monte Carlo realizations of the data and refitting. However, interpolation can introduce significant errors in mixed-mode frequencies, particularly near avoided crossings, where the mode frequencies evolve rapidly with stellar evolution. (Clara et al. (2025); Li et al. (2020)).

Our primary goal was to investigate whether the inclusion of quadrupolar modes tightens the constraints on the inferred stellar parameters. For this purpose, we used a simpler approach to compare the constraints on stellar parameters with and without quadrupolar modes. We defined a model-selection criterion, $\overline{\chi}^2 \leq \overline{\chi}^2_{\rm min} + 1$, to select models close to the best-fit model, for which $\overline{\chi}^2 = \overline{\chi}^2_{\rm min}$. We then added the quadrupolar modes, recomputed the mean chi-square and examined how many of the previously acceptable models remained within the criterion. We then compared how the ranges of stellar parameters spanned by the selected models changed with the addition of quadrupolar modes. This effectively measures how much the additional seismic information tightens the constraints on stellar parameters.

We preferred the mean χ^2 over the reduced χ^2 as the selection metric for the following reasons. First, for non-linear models such as stellar models, the effective number of degrees of freedom is generally unknown, making the interpretation of the reduced χ^2 ambiguous (Andrae et al. 2010). The standard definition, $N-p$ (the number of observables minus the number of free parameters), is exact only for linear models. Second, to compare the relative constraining power of different sets of seismic observables, the mean χ^2 provides a more appropriate and consistent measure of the average misfit per observable.

We found that the number of models satisfying the selection criterion decreases substantially with the addition of quadrupolar modes; however, the change in the parameter ranges spanned by the selected models is very small (see Table 8). For the case with the cubic surface correction, the lower bounds on mass, age and radius change by $< 0.5\%$, whereas the upper bounds decrease by 0.1%, 3.5% and 0.03%, respectively. The 33 models satisfying the selection criterion $\overline{\chi}^2_{A01} \leq \overline{\chi}^2_{A01,\rm min} + 1$ are listed in Table 9. After including quadrupolar modes, only 19 of these 33 models remain acceptable under the criterion $\overline{\chi}^2_{A012} \leq \overline{\chi}^2_{A012,\rm min} + 1$. The remaining 14 rejected models are marked by (*).

The best-fit stellar parameters obtained with the cubic and combined surface correction are not very different (see Table 7); however, the parameter ranges spanned by the models satisfying the selection criterion are much broader for the case of combined surface correction (see Table 8). This is because the additional degree of freedom can overcorrect models that are far from the true model. Therefore, for comparing the constraints on stellar parameters, we consider only the case with the cubic surface correction.

4.2.4. *Parameter degeneracy and helium enrichment constraint*

Due to parameter degeneracy, many combinations of the six free parameters (mass, age, $Y_{\rm in}$, $[{\rm M/H}]_{\rm in}$, $\alpha_{\rm CGM}$, and the surface correction coefficient) reproduce the oscillation frequencies with very similar $\overline{\chi}^2$ values. The top models listed in Table 9 illustrate this multidimensional parameter degeneracy and, in particular, show a mass–helium anti-correlation (Nsamba et al. (2021); Li et al. (2020)). Among the top 10 models, the models with higher masses in the range $0.858 - 0.873\,{\rm M}_\odot$ have lower initial helium fractions, ranging from $0.247 - 0.252$, whereas the models with lower masses in the range $0.818 - 0.829\,{\rm M}_\odot$ have higher initial helium fractions, ranging from $0.264 - 0.273$.

Imposing the helium enrichment law constraint, discussed in Section 3.3.1, substantially reduces the parameter degeneracy (see Table 8), leaving only 7 models (4 with the cubic correction and 3 with the combined correction) that satisfy the selection criterion $\chi^2_{A01} \leq \overline{\chi}^2_{A01,\rm min} + 1$ & $\overline{\chi}^2_{A012} \leq \overline{\chi}^2_{A012,\rm min} + 1$. However, the helium enrichment law is an additional assumption and may not be appropriate if the star formed in a helium-enhanced environment or followed a non-standard evolutionary pathway.. These seven models span mass, age and radius ranges of $0.858 - 0.873\,{\rm M}_\odot$, $8.67 - 9.24\,{\rm Gyr}$, $2.65 - 2.67\,{\rm R}_\odot$, respectively. Similar to Deheuvels, S. et al. (2012), we adopted a primordial helium abundance of $Y_p = 0.2477$ (Peimbert et al. 2007), and used a helium-to-metal enrichment ratio in the range $1 \leq \Delta Y/\Delta Z \leq 5$ (Pagel & Portinari (1998)), which encompasses all the values reported in the literature (Nsamba et al. (2021)). Table 7 also shows the best-fit parameter values after applying the helium enrichment law constraint.

5. DISCUSSION

Section 4.2.2 shows that, after including quadrupolar modes, the best-fit mass, age and radius change by 0.2%, 1.7% and 0.4%, respectively. Moreover, Section 4.2.3 shows that the upper and lower bounds of the parameter ranges spanned by the selected models change by only very small percentages. Changes of $\lesssim 1\%$ in the upper and lower bounds of the mass range do not provide compelling evidence for an improvement in the stellar constraints. Such small changes could arise due to other technical factors, such as uneven sampling of the parameter space by the level-set GPO code, or limitations of the first-order surface corrections for quadrupolar modes undergoing avoided crossings (Joel Ong et al. 2021). Hence, our analysis shows that the inclusion of quadrupolar modes did not significantly improve the constraints on stellar parameters for KIC 7341231.

The quadrupolar mixed modes that are near avoided crossings are not well reproduced by the best-fit models. This discrepancy is possibly due to systematic errors in the surface correction. Joel Ong et al. (2021) showed that first-order perturbation for surface corrections may not be sufficient when the surface-correction term is comparable to the coupling strength, which is the case for quadrupolar modes near avoided crossings.

The mismatch between the observed and model frequencies of the modes showing strong NDE also reflects in the mixing fraction $\zeta_2(\nu_i)$ (see Figure 10). The asymptotic relation between $\zeta_2(\nu_i)$ and the mixed-mode frequencies is given by Equation 8. This was used to compute the observed $\zeta_2(\nu_i)$. For the MESA models, $\zeta_2(\nu_i)$ was computed as the ratio of the mode inertia contributed by the g-mode cavity to the total mode inertia, which is computed by GYRE. The models shown in Figure 10 correspond to the best-fit models shown in Figures 6b and 7b, and the corresponding observed values are also plotted. The best-fit models fail to match $\zeta_2(\nu_i)$ for the quadrupolar mixed modes exhibiting strong NDE. A detailed investigation of this discrepancy is not within the scope of the present work.

Additionally, Figure 11 in the Appendix illustrates the temporal evolution of the mixing fraction, $\zeta_2(\nu_i)$, across the avoided crossings, in time steps of 0.5 Myr. As expected, $\zeta_2(\nu_i)$ varies sharply during avoided crossings.

Figures 6 and 7 show that the best-fit models reproduce the quadrupolar frequencies in reasonable agreement with the observed values. Even the g-dominated modes obtained from the asymptotic MCMC fit, which are not visible in the oscillation spectrum and were therefore not used as observational constraints, are reproduced fairly well by the best-fit models. Notably, the best-fit models obtained using only the radial and dipolar modes also fit these modes reasonably well. This suggests that the asymptotic seismic parameters $\delta\nu_{02}$, $\Delta\Pi_2$, and $\epsilon_{g,2}$ are likely correlated with the asymptotic parameters $\Delta\nu$, $\delta\nu_{01}$, $\Delta\Pi_1$, and $\epsilon_{g,1}$. $\Delta\Pi_2$ and $\Delta\Pi_1$ are related through the theoretical asymptotic relation given by equation 26, and the empirical scaling relation between $\delta\nu_{02}$ and $\Delta\nu$ is well established (Huber et al. 2010). However, no theoretical or empirical relation involving $\epsilon_{g,2}$ has yet been reported. Apart from this work, so far only two measurements of $\epsilon_{g,2}$ have been reported in the literature (Liagre et al. 2025).

6. SUMMARY

In this work, we performed a global asymptotic fit of the quadrupolar mixed modes of a young red giant KIC 7341231, whose rotational multiplets exhibit strong NDE. We applied the implicit approach introduced by Li et al. (2024), in which rotational perturbations are added to the uncoupled p- and g-mode frequencies prior to solving the mixed-mode coupling equation. This approach is applied here for the first time to quadrupolar mixed modes. The resulting best-fit seismic parameters are in good agreement with the values reported in a recent study by Liagre et al. (2025), who used a different methodology in which rotational perturbations are added after computing the mixed-mode frequencies. This agreement demonstrates the consistency of the two independent methodologies for modeling quadrupolar mixed modes in evolved solar-like stars.

The global MCMC fit of the quadrupolar modes yielded precise estimates of q_2, $\Delta\Pi_2$, $\epsilon_{g,2}$, $\delta\nu_{02}$, and the envelope rotation rate. The envelope rotation rate inferred from the $\ell = 2$ modes is consistent, within uncertainties, with that obtained from the dipolar mixed modes.

Another primary goal of this work was to investigate the impact of quadrupolar modes on the constraints on stellar parameters beyond those provided by radial modes and dipolar mixed modes. For this, we carried out GPO-based stellar modeling using MESA and GYRE. The observed frequencies of the $\ell = 0$, 1, and 2 modes, together with the atmospheric observables T_{eff} and surface metallicity, were used as observational constraints. We compared the inferred stellar parameters obtained with and without the inclusion of quadrupolar modes.

For KIC 7341231, including quadrupolar modes did not significantly change the inferences. This suggests that, for evolved solar-like stars such as KIC 7341231, with well-characterized dipolar mixed modes, radial and dipolar modes may already provide sufficient constraints on the stellar parameters. However, in stars with detectable glitch signatures, the potential contribution of quadrupolar modes to stellar modeling may be more significant.

Table 7: Best-fit stellar models obtained with and without including quadrupolar modes in the χ^2 analysis. $\overline{\chi}^2_{A01}$ denotes the mean chi-square computed using radial and dipolar modes, along with the atmospheric observables, while $\overline{\chi}^2_{A012}$ additionally includes the quadrupolar modes. Results are shown for both the cubic and combined (cubic+inverse) surface corrections. The lower half of the table lists the corresponding best-fit models after imposing the helium enrichment law constraint described in Section 4.2.4.

Best-fit model	**Surface correction**	$\overline{\chi}^2_{A01}$	$\overline{\chi}^2_{A012}$
Excluding $\ell = 2$ modes			
$\mathrm{M} = 0.859\,\mathrm{M}_\odot$, Age $= 9.04\,$Gyr, $Y_{\rm in} = 0.251$, $[\mathrm{M/H}]_{\rm in} = -1.53\,$dex, $\mathrm{R} = 2.66\,\mathrm{R}_\odot$, $T_{\rm eff} = 5816\,K$, $\log g = 3.52$, $\log(L/L_\odot) = 0.862$, $\alpha_{\rm CGM} = 1.41$	cubic	3.1	5.0
Including $\ell = 2$ modes			
$\mathrm{M} = 0.857\,\mathrm{M}_\odot$, Age $= 8.89\,$Gyr, $Y_{\rm in} = 0.255$, $[\mathrm{M/H}]_{\rm in} = -1.53\,$dex, $\mathrm{R} = 2.65\,\mathrm{R}_\odot$, $T_{\rm eff} = 5836\,K$, $\log g = 3.52$, $\log(L/L_\odot) = 0.867$, $\alpha_{\rm CGM} = 1.44$		3.5	4.7
Excluding $\ell = 2$ modes			
$\mathrm{M} = 0.859\,\mathrm{M}_\odot$, Age $= 9.20\,$Gyr, $Y_{\rm in} = 0.248$, $[\mathrm{M/H}]_{\rm in} = -1.53\,$dex, $\mathrm{R} = 2.66\,\mathrm{R}_\odot$, $T_{\rm eff} = 5794\,K$, $\log g = 3.52$, $\log(L/L_\odot) = 0.855$, $\alpha_{\rm CGM} = 1.37$	combined	2.5	3.7
Including $\ell = 2$ modes			
$\mathrm{M} = 0.856\,\mathrm{M}_\odot$, Age $= 8.87\,$Gyr, $Y_{\rm in} = 0.256$, $[\mathrm{M/H}]_{\rm in} = -1.53\,$dex, $\mathrm{R} = 2.65\,\mathrm{R}_\odot$, $T_{\rm eff} = 5838\,K$, $\log g = 3.52$, $\log(L/L_\odot) = 0.868$, $\alpha_{\rm CGM} = 1.44$		2.6	3.1
With the helium enrichment law constraint:			
Excluding $\ell = 2$ modes			
$\mathrm{M} = 0.858\,\mathrm{M}_\odot$, Age $= 9.24\,$Gyr, $Y_{\rm in} = 0.248$, $[\mathrm{M/H}]_{\rm in} = -1.53\,$dex, $\mathrm{R} = 2.65\,\mathrm{R}_\odot$, $T_{\rm eff} = 5792\,K$, $\log g = 3.52$, $\log(L/L_\odot) = 0.854$, $\alpha_{\rm CGM} = 1.37$	cubic	3.3	6.1
Including $\ell = 2$ modes			
$\mathrm{M} = 0.858\,\mathrm{M}_\odot$, Age $= 9.13\,$Gyr, $Y_{\rm in} = 0.250$, $[\mathrm{M/H}]_{\rm in} = -1.53\,$dex, $\mathrm{R} = 2.66\,\mathrm{R}_\odot$, $T_{\rm eff} = 5805\,K$, $\log g = 3.52$, $\log(L/L_\odot) = 0.858$, $\alpha_{\rm CGM} = 1.39$		3.8	5.2
Excluding $\ell = 2$ modes			
Same model as without the helium enrichment law constraint.	combined		
Including $\ell = 2$ modes			
Same model as excluding $\ell = 2$ modes.			

Table 8: Ranges of stellar parameters spanned by the models satisfying the selection criteria. Results are presented for both the cubic and combined (cubic+inverse) surface corrections. The lower half of the table shows the corresponding parameter ranges after imposing the helium enrichment law constraint described in Section 4.2.4.

Constraints	**Surface correction**	**No. of models**	**Mass** ($M_\odot$)	**Age** (Gyr)	**Radius** ($R_\odot$)	$[M/H]_{\rm in}$ (dex)
$\overline{\chi}^2_{A01} \leq \overline{\chi}^2_{A01,\rm min} + 1$	cubic	33	$0.814 - 0.895$	$7.53 - 9.70$	$2.61 - 2.69$	-1.65–-1.15
$\overline{\chi}^2_{A01} \leq \overline{\chi}^2_{A01,\rm min} + 1$ **&** $\overline{\chi}^2_{A012} \leq \overline{\chi}^2_{A012,\rm min} + 1$		19	$0.818 - 0.894$	$7.53 - 9.36$	$2.61 - 2.69$	-1.65–-1.15
$\overline{\chi}^2_{A01} \leq \overline{\chi}^2_{A01,\rm min} + 1$	combined	77	$0.769 - 0.880$	$7.61 - 10.79$	$2.56 - 2.68$	-1.66–-1.20
$\overline{\chi}^2_{A01} \leq \overline{\chi}^2_{A01,\rm min} + 1$ **&** $\overline{\chi}^2_{A012} \leq \overline{\chi}^2_{A012,\rm min} + 1$		31	$0.769 - 0.873$	$8.31 - 10.02$	$2.56 - 2.67$	-1.66–-1.26
With the helium enrichment law constraint:						
$\overline{\chi}^2_{A01} \leq \overline{\chi}^2_{A01,\rm min} + 1$	cubic	5	$0.858 - 0.873$	$8.67 - 9.24$	$2.65 - 2.67$	-1.53–-1.43
$\overline{\chi}^2_{A01} \leq \overline{\chi}^2_{A01,\rm min} + 1$ **&** $\overline{\chi}^2_{A012} \leq \overline{\chi}^2_{A012,\rm min} + 1$		4	$0.858 - 0.873$	$8.67 - 9.24$	$2.65 - 2.67$	-1.53–-1.43
$\overline{\chi}^2_{A01} \leq \overline{\chi}^2_{A01,\rm min} + 1$	combined	9	$0.824 - 0.873$	$8.67 - 10.57$	$2.62 - 2.67$	-1.53–-1.43
$\overline{\chi}^2_{A01} \leq \overline{\chi}^2_{A01,\rm min} + 1$ **&** $\overline{\chi}^2_{A012} \leq \overline{\chi}^2_{A012,\rm min} + 1$		3	$0.859 - 0.872$	$8.70 - 9.20$	$2.66 - 2.67$	-1.53–-1.43

Table 8 continued.

Constraints	**Surface correction**	$T_{\rm eff}$ (K)	$\log g$	$\log\left(\frac{L}{L_\odot}\right)$	$Y_{\rm in}$	$\alpha_{\rm \mathbf{CGM}}$
$\overline{\chi}^2_{A01} \leq \overline{\chi}^2_{A01,\rm min} + 1$	cubic	$5772 - 5877$	$3.52 - 3.53$	$0.838 - 0.884$	$0.241 - 0.297$	$1.33 - 1.50$
$\overline{\chi}^2_{A01} \leq \overline{\chi}^2_{A01,\rm min} + 1$ **&** $\overline{\chi}^2_{A012} \leq \overline{\chi}^2_{A012,\rm min} + 1$		$5805 - 5877$	$3.52 - 3.53$	$0.850 - 0.884$	$0.250 - 0.297$	$1.39 - 1.50$
$\overline{\chi}^2_{A01,\rm min} + 1$	combined	$5680 - 5877$	$3.51 - 3.53$	$0.794 - 0.877$	$0.240 - 0.299$	$1.16 - 1.48$
$\overline{\chi}^2_{A01} \leq \overline{\chi}^2_{A01,\rm min} + 1$ **&** $\overline{\chi}^2_{A012} \leq \overline{\chi}^2_{A012,\rm min} + 1$		$5770 - 5865$	$3.51 - 3.52$	$0.819 - 0.877$	$0.243 - 0.298$	$1.28 - 1.48$
With the helium enrichment law constraint:						
$\overline{\chi}^2_{A01} \leq \overline{\chi}^2_{A01,\rm min} + 1$	cubic	$5792 - 5806$	$3.52 - 3.53$	$0.854 - 0.863$	$0.248 - 0.250$	$1.37 - 1.41$
$\overline{\chi}^2_{A01} \leq \overline{\chi}^2_{A01,\rm min} + 1$ **&** $\overline{\chi}^2_{A012} \leq \overline{\chi}^2_{A012,\rm min} + 1$		$5792 - 5806$	$3.52 - 3.53$	$0.854 - 0.863$	$0.248 - 0.250$	$1.37 - 1.41$
$\overline{\chi}^2_{A01,\rm min} + 1$	combined	$5680 - 5810$	$3.52 - 3.53$	$0.809 - 0.863$	$0.248 - 0.250$	$1.17 - 1.41$
$\overline{\chi}^2_{A01} \leq \overline{\chi}^2_{A01,\rm min} + 1$ **&** $\overline{\chi}^2_{A012} \leq \overline{\chi}^2_{A012,\rm min} + 1$		$5794 - 5810$	3.52	$0.855 - 0.862$	$0.248 - 0.250$	$1.37 - 1.40$

Table 9: All 33 stellar models satisfying the selection criterion $\overline{\chi}^2_{A01} \leq \overline{\chi}^2_{A01,\mathrm{min}} + 1$ (see the first row of Table 8), together with the corresponding values of $\overline{\chi}^2_{A01}$ and $\overline{\chi}^2_{A012}$. The models are listed in ascending order of $\overline{\chi}^2_{A01}$. $\delta\nu_{\mathrm{surf,max}}$ denotes the surface correction obtained for the highest-order radial mode (531.52 μHz) used in the analysis. Models marked with an asterisk (*) do not satisfy the selection criterion after including the quadrupolar modes, i.e., $\overline{\chi}^2_{A012} \leq \overline{\chi}^2_{A012,\mathrm{min}} + 1$. The values of $\Delta\nu_{\mathrm{mod}}$ $\epsilon_{p,\mathrm{mod}}$ were obtained by fitting the radial-mode frequencies using Equation 1, as described in Section 3.3.4, while $\Delta\Pi_{\mathrm{mod}}$ was computed by MESA using the asymptotic relation given in Equation 26. The values of $\Delta\Pi_{\mathrm{mod}}$ differ from the observed value obtained from the MCMC fit, 111.23 s. This is because MESA computes $\Delta\Pi_{\mathrm{mod}}$ using a theoretical asymptotic expression (equation 26), whose underlying assumptions are not valid for subgiants and young red giants (Deheuvels, S. et al. (2015)).

Mass ($M_\odot$)	**Age** (Gyr)	Y_{in}	[M/H]$_{\mathrm{in}}$ (dex)	α_{CGM}	$\delta\nu_{\mathrm{surf,max}}$ (μHz)	$\overline{\chi}^2_{A01}$	$\overline{\chi}^2_{A012}$	$\Delta\nu_{\mathrm{mod}}$ (μHz)	$\epsilon_{p,\mathrm{mod}}$	$\Delta\Pi_{\mathrm{mod}}$ (s)
0.859	9.04	0.251	-1.53	1.41	-3.40	3.13	5.02	29.02	0.246	115.14
0.829	9.36	0.264	-1.65	1.44	-3.91	3.19	5.24	29.02	0.249	115.11
0.873	8.62	0.251	-1.43	1.42	-3.24	3.21	5.15	29.01	0.255	115.14
*0.858	9.29	0.247	-1.53	1.36	-3.88	3.22	6.44	29.01	0.256	115.13
*0.858	9.24	0.248	-1.53	1.37	-3.71	3.26	6.06	29.02	0.251	115.14
0.873	8.57	0.252	-1.43	1.43	-3.12	3.26	4.83	29.01	0.252	115.15
0.861	8.96	0.251	-1.53	1.42	-3.21	3.32	4.75	29.03	0.242	115.13
0.818	9.36	0.273	-1.52	1.39	-3.95	3.39	5.60	29.02	0.249	115.07
*0.859	9.15	0.249	-1.53	1.39	-3.86	3.42	6.47	29.00	0.257	115.13
0.873	8.67	0.250	-1.43	1.41	-3.32	3.49	5.52	29.00	0.255	115.14
0.819	8.75	0.286	-1.33	1.40	-3.38	3.51	4.87	29.02	0.248	115.04
0.857	8.89	0.255	-1.53	1.44	-3.09	3.54	4.70	29.04	0.240	115.13
*0.819	8.64	0.288	-1.33	1.43	-3.84	3.57	5.73	28.99	0.266	115.03
0.859	8.98	0.252	-1.53	1.42	-3.39	3.58	4.99	29.02	0.247	115.11
0.858	9.07	0.251	-1.53	1.40	-3.18	3.60	4.99	29.04	0.239	115.12
*0.828	9.29	0.266	-1.65	1.46	-4.18	3.64	6.55	29.00	0.258	115.11
*0.881	8.82	0.242	-1.44	1.37	-3.28	3.67	5.93	29.01	0.252	115.15
0.819	8.38	0.293	-1.33	1.48	-3.15	3.74	4.94	29.02	0.250	115.06
*0.873	8.72	0.249	-1.43	1.40	-3.42	3.76	5.84	29.00	0.257	115.13
0.857	9.00	0.253	-1.53	1.42	-3.65	3.81	5.58	29.00	0.254	115.12
*0.873	9.02	0.242	-1.54	1.40	-3.50	3.82	6.70	29.01	0.252	115.17
0.858	9.13	0.250	-1.53	1.39	-3.34	3.84	5.20	29.03	0.242	115.12
*0.818	8.76	0.288	-1.26	1.35	-3.69	3.84	5.89	29.00	0.259	115.02
0.818	8.62	0.289	-1.33	1.43	-3.12	3.84	4.75	29.03	0.243	115.04
0.828	9.35	0.265	-1.65	1.44	-3.54	3.87	4.94	29.04	0.239	115.10
*0.881	8.87	0.241	-1.44	1.36	-3.47	3.91	6.75	29.00	0.257	115.15
0.894	7.86	0.254	-1.35	1.50	-2.55	3.93	5.57	29.01	0.255	115.17
*0.815	9.60	0.271	-1.52	1.35	-4.10	3.97	5.95	29.02	0.247	115.04
*0.820	9.05	0.280	-1.34	1.34	-3.61	4.00	5.88	29.02	0.249	115.05
*0.895	8.27	0.245	-1.36	1.41	-2.92	4.03	6.05	29.00	0.257	115.16
0.873	8.41	0.255	-1.43	1.46	-2.44	4.05	4.88	29.04	0.236	115.13
0.845	7.53	0.297	-1.15	1.47	-2.62	4.07	5.27	29.00	0.260	115.06
*0.814	9.70	0.270	-1.52	1.33	-3.97	4.12	6.25	29.03	0.241	115.06

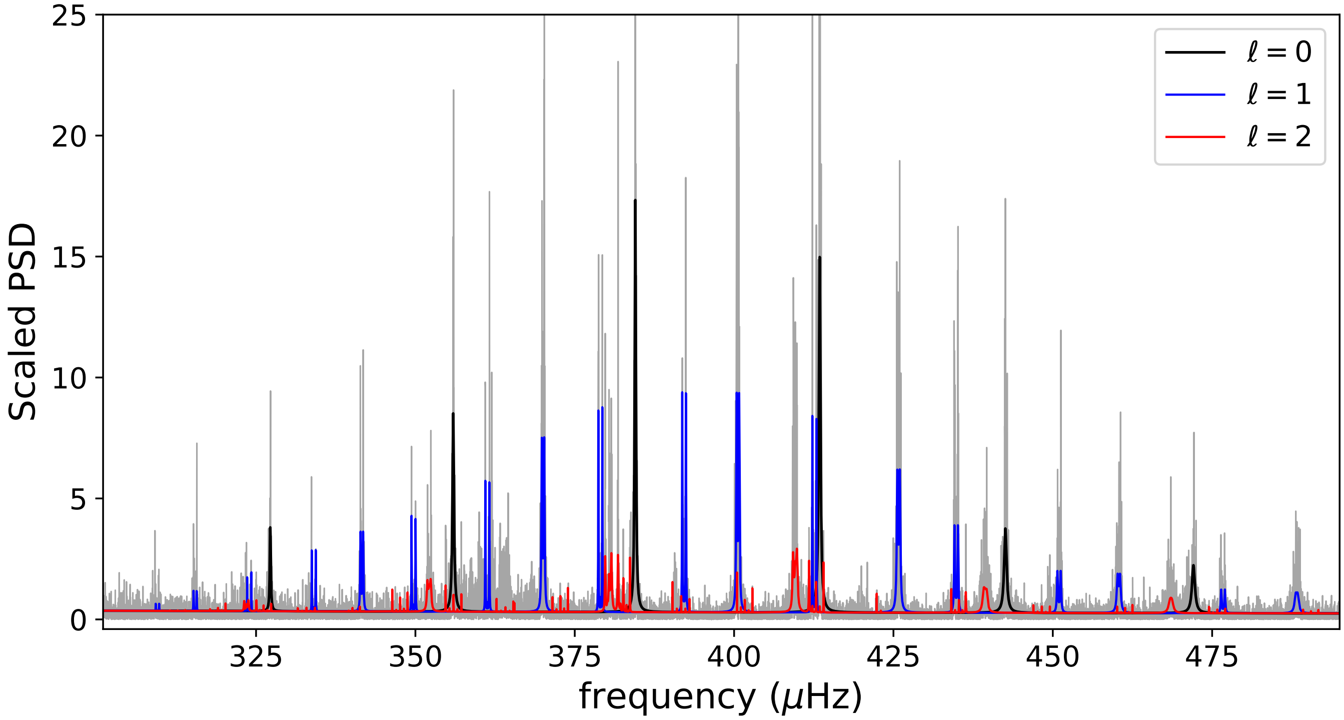

Figure 1: MCMC fit for KIC 7341231, with the power spectrum in grey. The $\ell = 0$, $\ell = 1$ and $\ell = 2$ modes are plotted in black, blue and red, respectively.

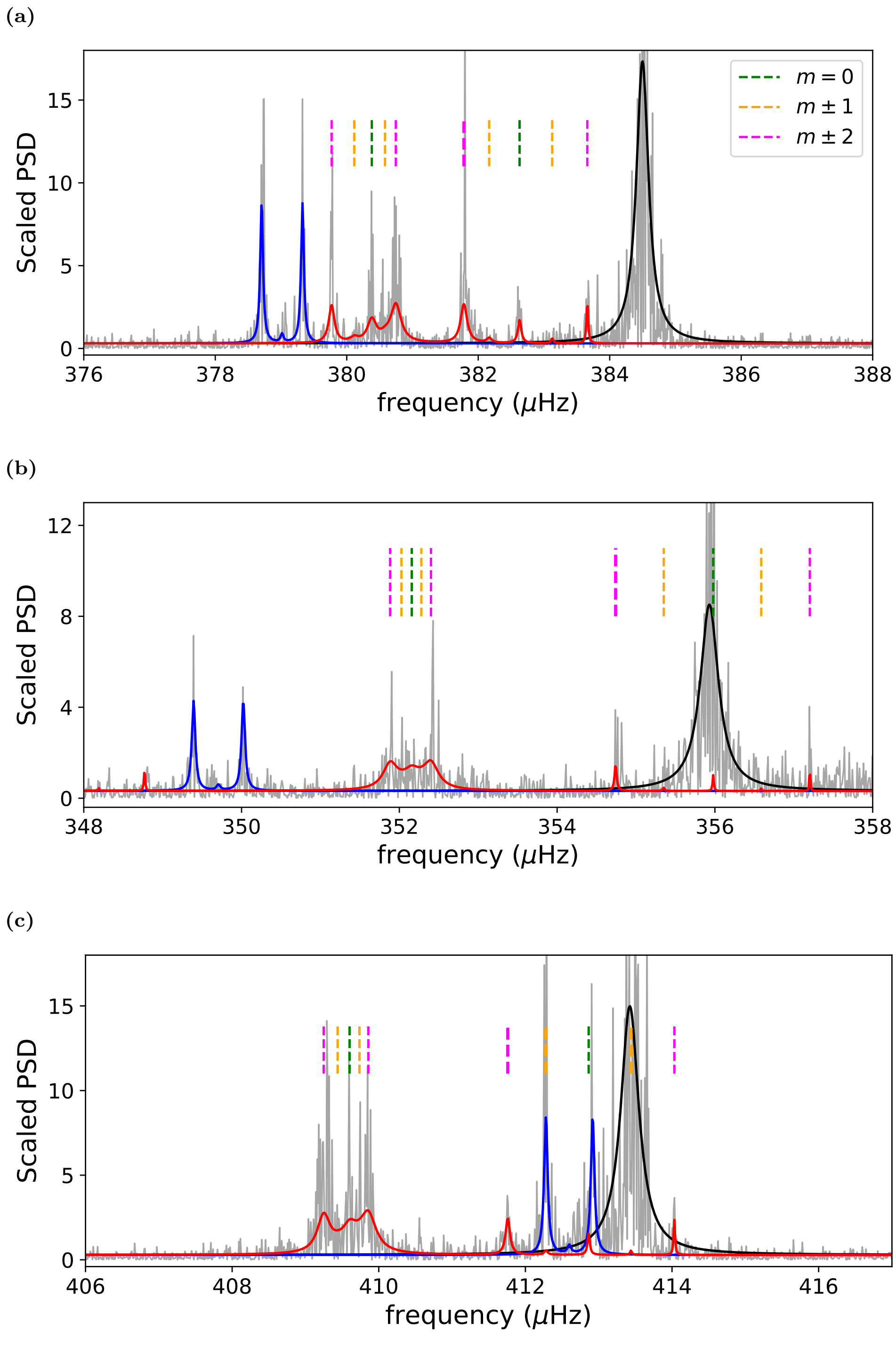

Figure 2: Zoomed-in plots for three radial orders around $\nu_{\max}$. The $\ell = 0$, $\ell = 1$ and $\ell = 2$ modes are plotted in black, blue and red, respectively. $m = 0$, $m = \pm 1$ and $m = \pm 2$ quadrupolar modes are marked with green, orange and magenta lines, respectively. Each m mode has a different linewidth because the linewidth is a function of the mixing fraction ζ, and each m mode has a different ζ.

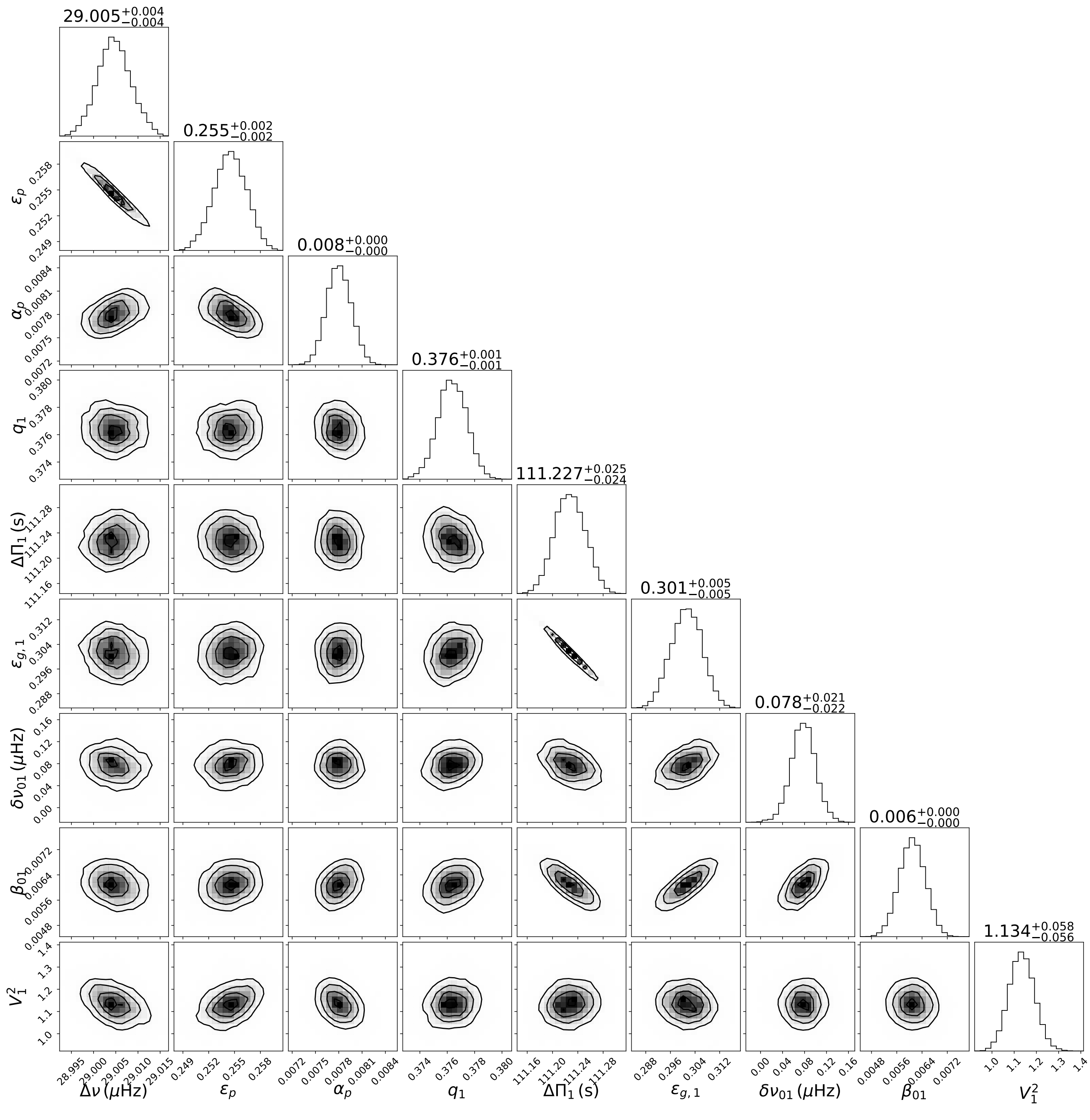

Figure 3: Corner plot of all global parameters of the $\ell = 0, 1$ MCMC fit (part 1). The median values are shown above the 1D histograms, along with $\pm 1\sigma$ uncertainties.

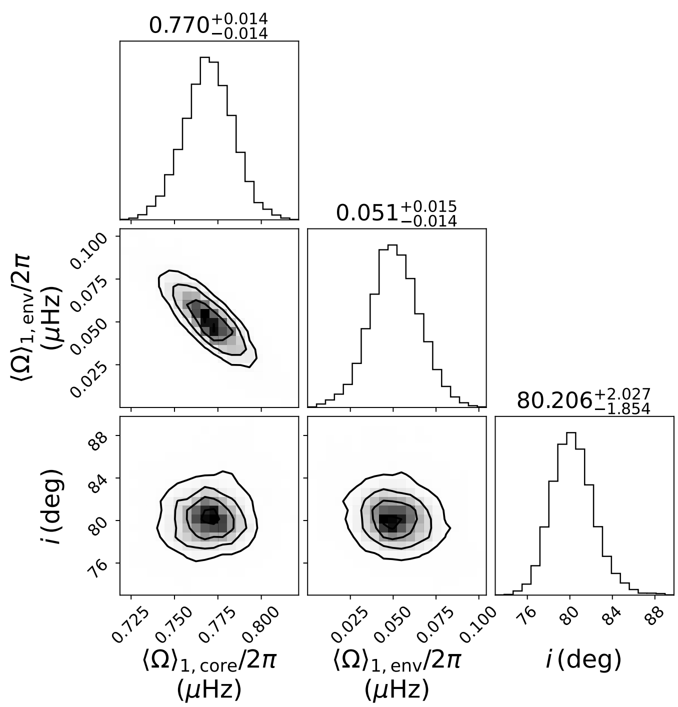

Figure 3: Corner plot of all global parameters of the $\ell = 0, 1$ MCMC fit (part 2).

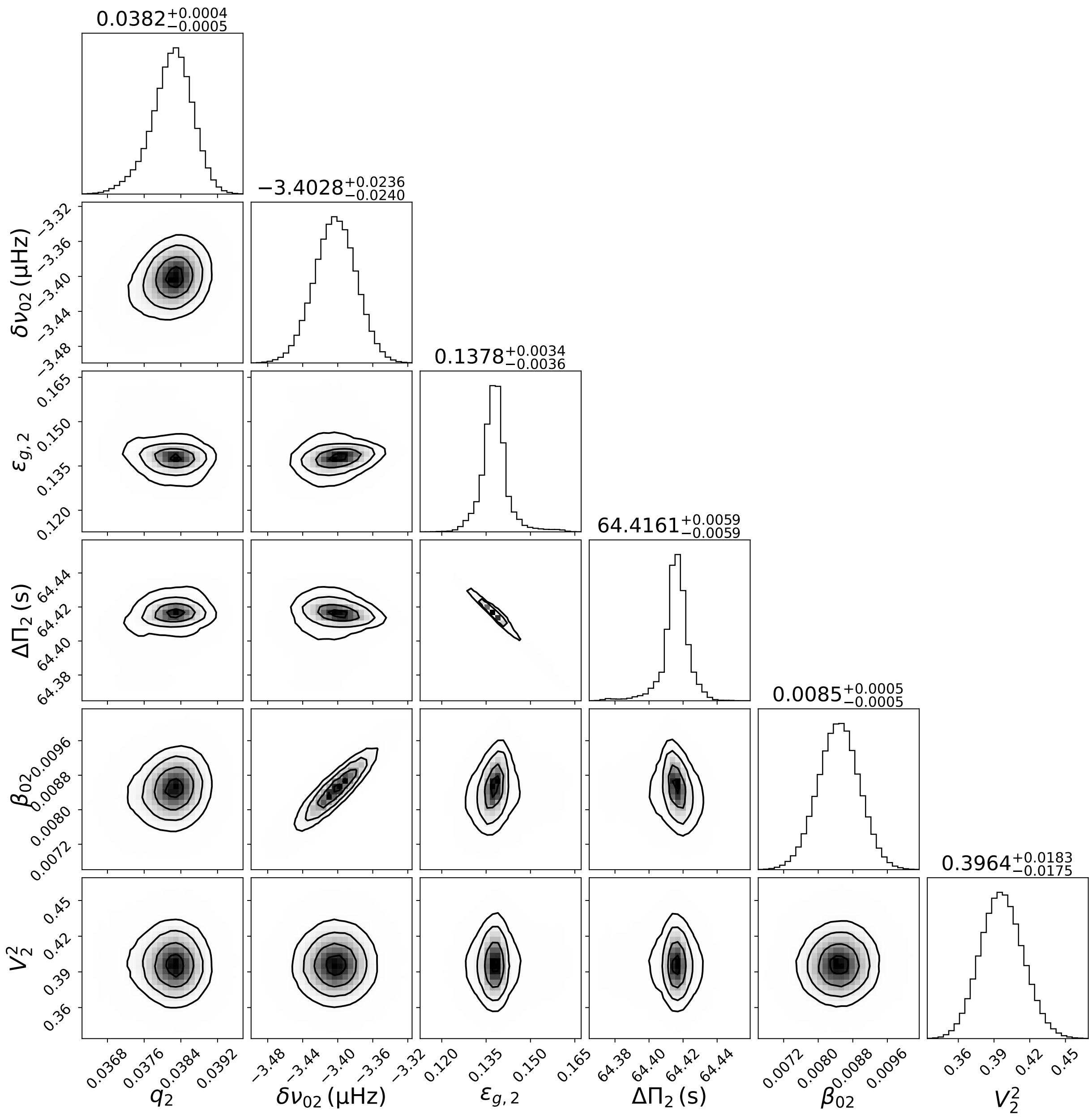

Figure 4: Corner plot of all parameters of the $\ell = 2$ fit with fixed core and envelope rotation.

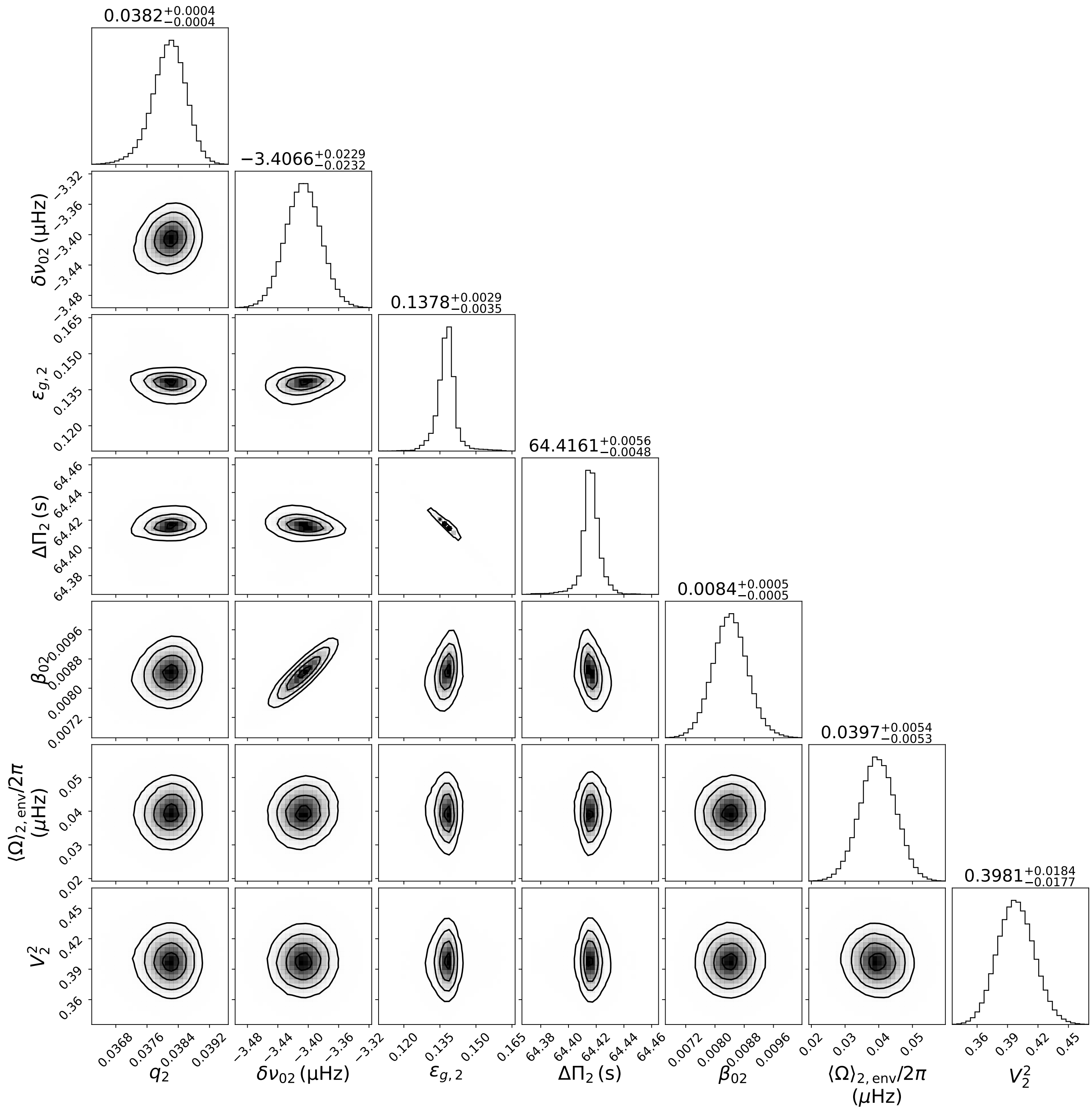

Figure 5: Corner plot of all parameters of the $\ell = 2$ fit with free envelope rotation.

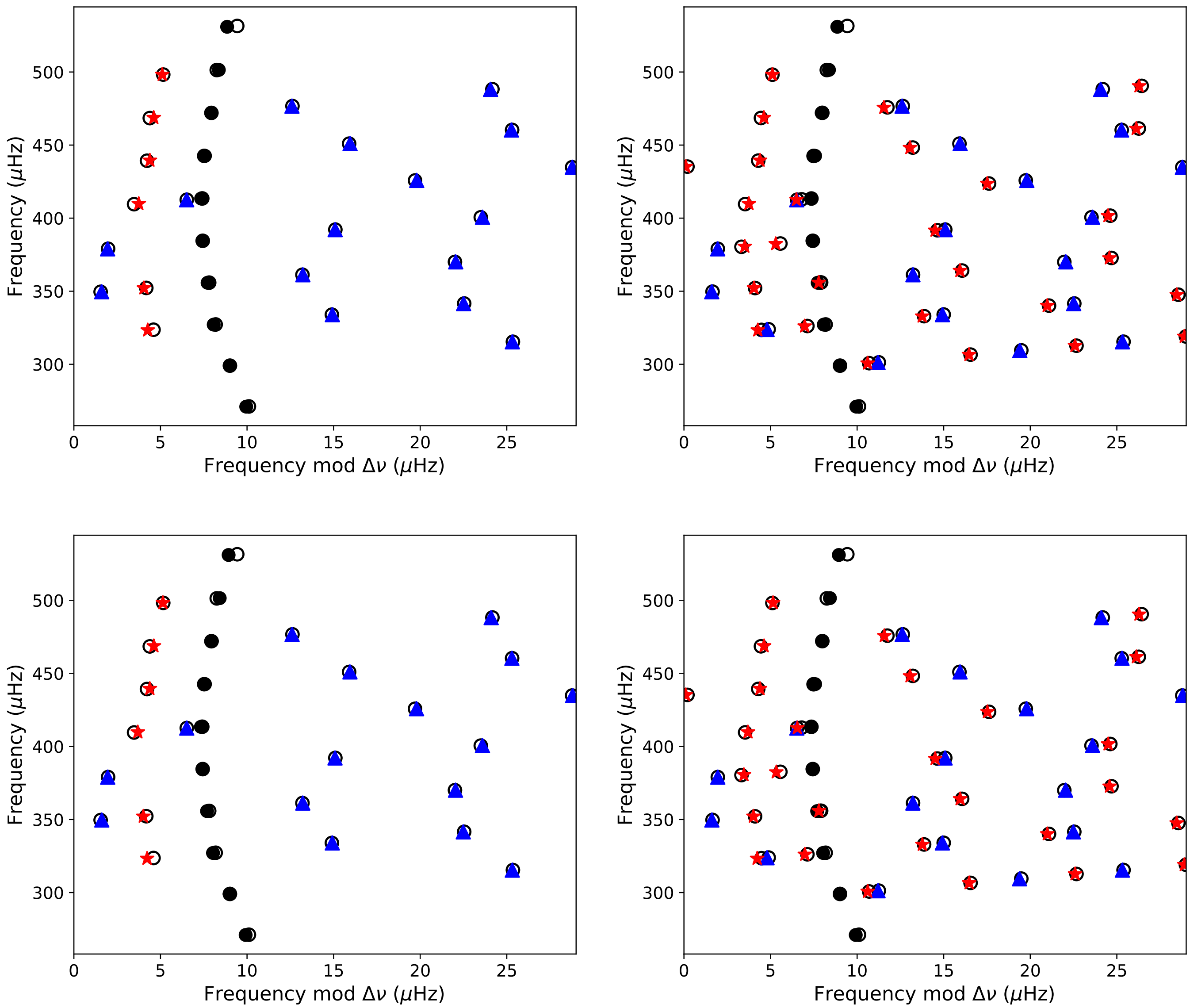

Figure 6: Échelle diagrams for the best-fit stellar models obtained without (**top**) and with (**bottom**) the inclusion of quadrupolar modes in the χ^2 analysis, for the case with cubic surface correction. The **left** plots compare the model frequencies with the locally fitted frequencies from Deheuvels, S. et al. (2012), while the **right** plots compare them with the frequencies obtained from the asymptotic fit to the observed spectrum performed in this work. The locally-fitted measurements were used to constrain the stellar models. The $\ell = 0$, 1 and 2 model frequencies are shown as solid black circles, blue triangles and red stars, respectively, while the observed/asymptotic-fit frequencies are shown as open black circles.

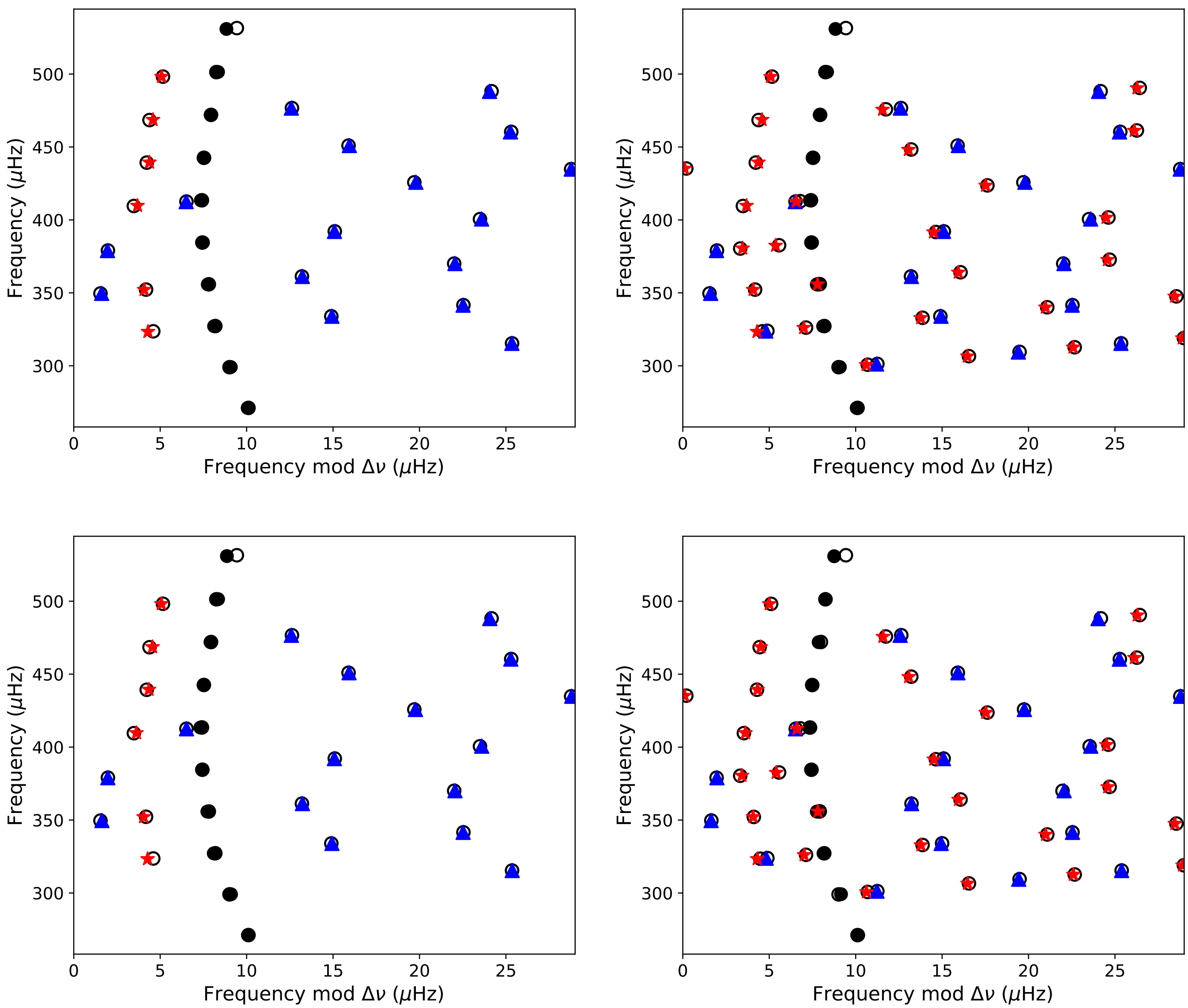

Figure 7: The caption is the same as that of Figure 6, but for the case with the combined (cubic +inverse) surface correction.

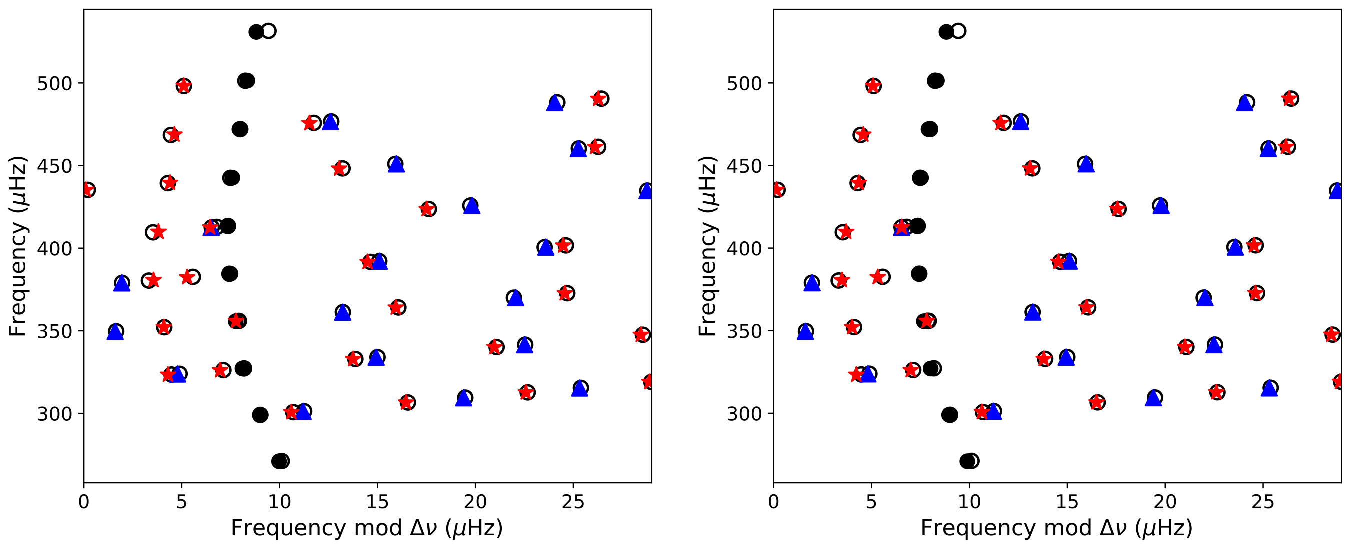

Figure 8: Échelle diagrams for the best-fit stellar models obtained without (**left**) and with (**right**) the inclusion of quadrupolar modes in the χ^2 analysis, after applying the helium enrichment law constraint. This is for the case with cubic surface correction. The colors and symbols used to plot the model and asymptotic-fit frequencies follow the same convention as in Figure 6.

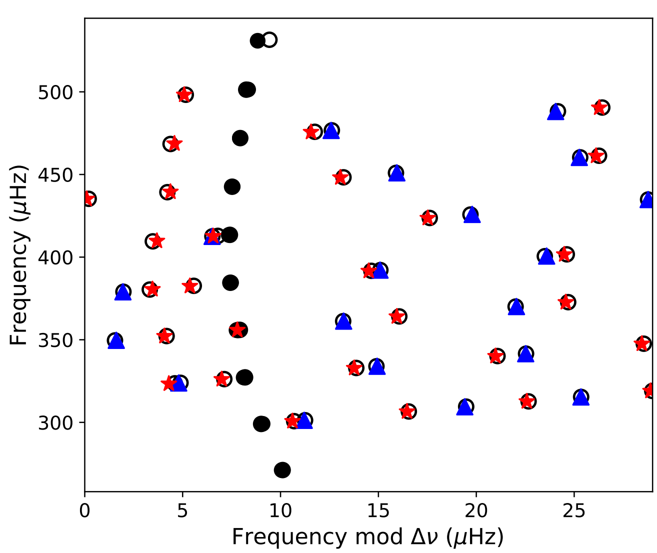

Figure 9: The caption is the same as that of Figure 8, but for the case with combined surface correction. The same best-fit model was obtained with and without the inclusion of quadrupolar modes.

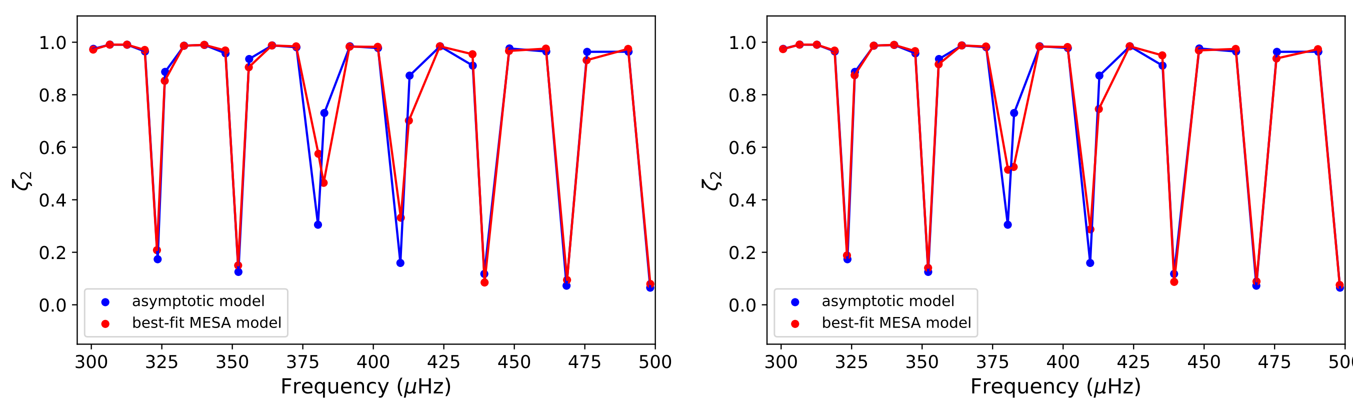

Figure 10: Mixing fraction $\zeta_2(\nu_i)$ as a function of the $\ell = 2$ mixed-mode frequencies for the best-fit stellar models (red), obtained with the inclusion of quadrupolar modes, for the cases with the cubic (**left**) and combined(**right**) surface corrections. The corresponding échelle diagrams are shown in Figures 6d and 7d, respectively. The observed values of $\zeta_2(\nu_i)$, obtained from the asymptotic fit to the observed spectrum, are also plotted in blue.

REFERENCES

Aerts, C., Christensen-Dalsgaard, J., & Kurtz, D. W. 2010, Asteroseismology, doi: 10.1007/978-1-4020-5803-5

Andrae, R., Schulze-Hartung, T., & Melchior, P. 2010, arXiv e-prints, arXiv:1012.3754, doi: 10.48550/arXiv.1012.3754

Appourchaux, T., Gizon, L., & Rabello-Soares, M.-C. 1998, Astron. Astrophys. Suppl. Ser., 132, 107, doi: 10.1051/aas:1998441

Appourchaux, T., Antia, H. M., Benomar, O., et al. 2014, AA, 566, A20, doi: 10.1051/0004-6361/201323317

Atchadé, Y. F. 2006, Methodology and Computing in Applied Probability, 8, 235, doi: 10.1007/s11009-006-8550-0

Ball, W. H., & Gizon, L. 2014, A&A, 568, A123, doi: 10.1051/0004-6361/201424325

Ball, W. H., Themeßl, N., & Hekker, S. 2018, MNRAS, 478, 4697, doi: 10.1093/mnras/sty1141

Ball, W. H., & Gizon, L. 2017, AA, 600, A128, doi: 10.1051/0004-6361/201630260

Beck, P. G., Bedding, T. R., Mosser, B., et al. 2011, Science, 332, 205, doi: 10.1126/science.1201939

Bedding, T. R., Huber, D., Stello, D., et al. 2010, ApJL, 713, L176, doi: 10.1088/2041-8205/713/2/L176

Benomar, O., Belkacem, K., Bedding, T. R., et al. 2014, The Astrophysical Journal Letters, 781, L29, doi: 10.1088/2041-8205/781/2/L29

Benomar, O., Bazot, M., Nielsen, M. B., et al. 2018, Science, 361, 1231, doi: 10.1126/science.aao6571

Benomar, O., Appourchaux, T., & Baudin, F. 2009, AA, 506, 15, doi: 10.1051/0004-6361/200911657

Brown, T. M., Gilliland, R. L., Noyes, R. W., & Ramsey, L. W. 1991, ApJ, 368, 599, doi: 10.1086/169725

Canuto, V. M., Goldman, I., & Mazzitelli, I. 1996, ApJ, 473, 550, doi: 10.1086/178166

Chaplin, W. J., & Miglio, A. 2013, ARA&A, 51, 353, doi: 10.1146/annurev-astro-082812-140938

Clara, M., Cunha, M. S., Avelino, P. P., et al. 2025, A&A, 694, A314, doi: 10.1051/0004-6361/202450514

Corsaro, E., McKeever, J. M., & Kuszlewicz, J. S. 2020, A&A, 640, A130, doi: 10.1051/0004-6361/202037930

Deheuvels, S., Ouazzani, R. M., & Basu, S. 2017, A&A, 605, A75, doi: 10.1051/0004-6361/201730786

Deheuvels, S., Ballot, J., Beck, P. G., et al. 2015, AA, 580, A96, doi: 10.1051/0004-6361/201526449

Deheuvels, S., et al. 2012, ApJ, 756, 19

Deheuvels, S., Dogan, G., Goupil, M. J., et al. 2014, A&A, 564, A27, doi: 10.1051/0004-6361/201322779

Frazier, P. I. 2018. https://arxiv.org/abs/1807.02811

García, R. A., & Ballot, J. 2019, Living Reviews in Solar Physics, 16, doi: 10.1007/s41116-019-0020-1

Gizon, L., & Solanki, S. 2004, Solar Phys., v.220, 169-184 (2004), 220, doi: 10.1023/B:SOLA.0000031378.29215.0c

Goodman, J., & Weare, J. 2010, Communications in Applied Mathematics and Computational Science, 5, 65, doi: 10.2140/camcos.2010.5.65

Goupil, M. J., Mosser, B., Marques, J. P., et al. 2013, A&A, 549, A75, doi: 10.1051/0004-6361/201220266

Harvey, J. 1985, in ESA Special Publication, Vol. 235, Future Missions in Solar, Heliospheric & Space Plasma Physics, ed. E. Rolfe & B. Battrick, 199

Hasan, S. S., Zahn, J.-P., & Christensen-Dalsgaard, J. 2005, AA, 444, L29, doi: 10.1051/0004-6361:200500203

Hastings, W. K. 1970, Biometrika, 57, 97, doi: 10.1093/biomet/57.1.97

Huber, D., Bedding, T. R., Stello, D., et al. 2010, ApJ, 723, 1607, doi: 10.1088/0004-637X/723/2/1607

Huber, D., Chaplin, W. J., Chontos, A., et al. 2019, 157, 245, doi: 10.3847/1538-3881/ab1488

Joel Ong, J. M., Basu, S., & Roxburgh, I. W. 2021, The Astrophysical Journal, 920, 8, doi: 10.3847/1538-4357/ac12ca

Jones, D. R., Schonlau, M., & Welch, W. J. 1998, Journal of Global Optimization, 13, 455, doi: 10.1023/A:1008306431147

Kallinger, T., De Ridder, J., Hekker, S., et al. 2014, A&A, 570, A41, doi: 10.1051/0004-6361/201424313

Li, G., Deheuvels, S., & Ballot, J. 2024, A&A, 688, A184, doi: 10.1051/0004-6361/202449882

Li, T., Bedding, T. R., Christensen-Dalsgaard, J., et al. 2020, Monthly Notices of the Royal Astronomical Society, 495, 3431, doi: 10.1093/mnras/staa1350

Li, T., Bedding, T. R., Huber, D., et al. 2017, Monthly Notices of the Royal Astronomical Society, 475, 981, doi: 10.1093/mnras/stx3079

Li, T., Davies, G. R., Nielsen, M., Cunha, M. S., & Lyttle, A. J. 2023, Monthly Notices of the Royal Astronomical Society, 523, 80, doi: 10.1093/mnras/stad1406

Li, T., Li, Y., Bi, S., et al. 2022, The Astrophysical Journal, 927, 167, doi: 10.3847/1538-4357/ac4fbf

Liagre, B., Desai, A., Einramhof, L., & Bugnet, L. 2025, Near-degeneracy effects in Quadrupolar Mixed Modes. From an Asymptotic Description to Data Fitting. https://arxiv.org/abs/2511.05314

Lund, M. N., Silva Aguirre, V., Davies, G. R., et al. 2017, ApJ, 835, 172, doi: 10.3847/1538-4357/835/2/172

Metropolis, N., Rosenbluth, A. W., Rosenbluth, M. N., Teller, A. H., & Teller, E. 1953, JChPh, 21, 1087, doi: 10.1063/1.1699114

Mosser, B., Gehan, C., Belkacem, K., et al. 2018, A&A, 618, A109, doi: 10.1051/0004-6361/201832777

Mosser, B., Belkacem, K., Goupil, M. J., et al. 2011, A&A, 525, L9, doi: 10.1051/0004-6361/201015440

Mosser, B., Elsworth, Y., Hekker, S., et al. 2012, A&A, 537, A30, doi: 10.1051/0004-6361/20111735210.1086/141952

Mosser, B., Goupil, M. J., Belkacem, K., et al. 2012b, A&A, 540, A143, doi: 10.1051/0004-6361/201118519

Murphy, S. J., Li, T., Sekaran, S., et al. 2021, Monthly Notices of the Royal Astronomical Society, 505, 2336, doi: 10.1093/mnras/stab1436

Nsamba, B., Moedas, N., Campante, T. L., et al. 2021, Monthly Notices of the Royal Astronomical Society, 500, 54, doi: 10.1093/mnras/staa3228

Ong, J. M. J., Bugnet, L., & Basu, S. 2022, The Astrophysical Journal, 940, 18, doi: 10.3847/1538-4357/ac97e7

Pagel, B. E. J., & Portinari, L. 1998, Monthly Notices of the Royal Astronomical Society, 298, 747, doi: 10.1046/j.1365-8711.1998.01637.x

Paxton, B., Bildsten, L., Dotter, A., et al. 2010, The Astrophysical Journal Supplement Series, 192, 3, doi: 10.1088/0067-0049/192/1/3

Paxton, B., Bildsten, L., Dotter, A., et al. 2011, ApJS, 192, 3, doi: 10.1088/0067-0049/192/1/3

Paxton, B., Cantiello, M., Arras, P., et al. 2013, ApJS, 208, 4, doi: 10.1088/0067-0049/208/1/4

Paxton, B., Marchant, P., Schwab, J., et al. 2015, ApJS, 220, 15, doi: 10.1088/0067-0049/220/1/15

Paxton, B., Schwab, J., Bauer, E. B., et al. 2018, ApJS, 234, 34, doi: 10.3847/1538-4365/aaa5a8

Paxton, B., Smolec, R., Schwab, J., et al. 2019, ApJS, 243, 10, doi: 10.3847/1538-4365/ab2241

Peimbert, M., Luridiana, V., & Peimbert, A. 2007, The Astrophysical Journal, 666, 636, doi: 10.1086/520571

Piau, L., Kervella, P., Dib, S., & Hauschildt, P. 2011, AA, 526, A100, doi: 10.1051/0004-6361/201014442

Pérez Hernández, F., García, R. A., Corsaro, E., Triana, S. A., & De Ridder, J. 2016, AA, 591, A99, doi: 10.1051/0004-6361/201628311

Samadi, R., Kupka, F., Goupil, M. J., Lebreton, Y., & C. van't Veer-Menneret. 2006, AA, 445, 233, doi: 10.1051/0004-6361:20052904

Sonoi, T., Ludwig, H.-G., Dupret, M.-A., et al. 2019, AA, 621, A84, doi: 10.1051/0004-6361/201833495

Townsend, R. H. D., & Teitler, S. A. 2013, MNRAS, 435, 3406, doi: 10.1093/mnras/stt1533

Unno, W., Osaki, Y., Ando, H., Saio, H., & Shibahashi, H. 1989, Nonradial oscillations of stars

Wang, Y., Li, T., Bi, S., Bedding, T. R., & Li, Y. 2023, The Astrophysical Journal, 953, 182, doi: 10.3847/1538-4357/ace4c9

APPENDIX

Table 10: Best-fit values of the background-model parameters and their associated 1-σ uncertainties.

Parameter	**Best-fit value**	**Unit**
N_0	5.75 ± 0.04	$\mathrm{ppm}^2\,\mu\mathrm{Hz}^{-1}$
τ_1	$(3.4 \pm 0.3) \times 10^5$	s
τ_2	$(1.34 \pm 0.01) \times 10^3$	s
τ_3	360.7 ± 0.7	s
a_1/b_1	$(3.4 \pm 0.6) \times 10^4$	$\mathrm{ppm}^2\,\mu\mathrm{Hz}^{-1}$
a_2/b_2	31.8 ± 0.3	$\mathrm{ppm}^2\,\mu\mathrm{Hz}^{-1}$
a_3/b_3	11.73 ± 0.02	$\mathrm{ppm}^2\,\mu\mathrm{Hz}^{-1}$

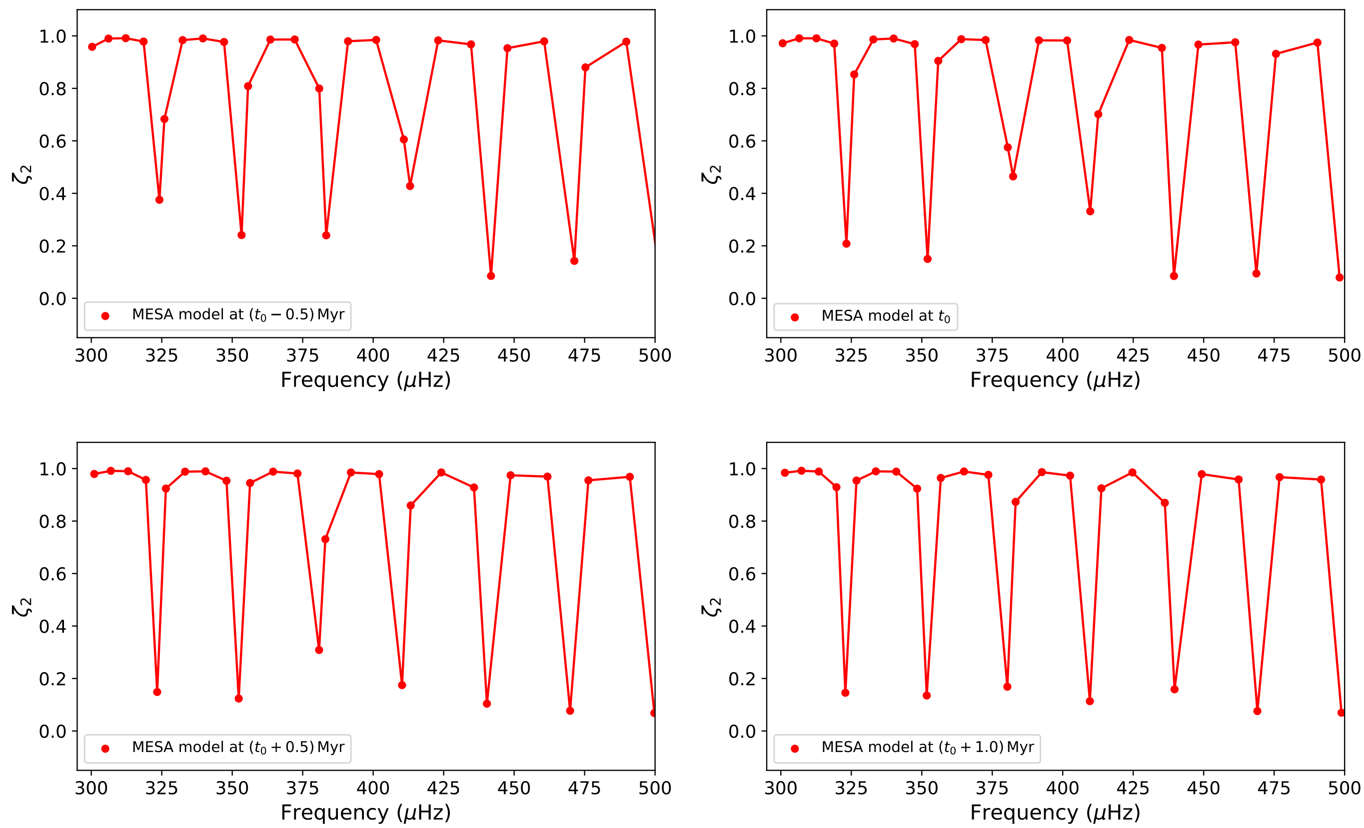

Figure 11: The temporal evolution of the mixing fraction $\zeta_2(\nu_i)$, shown at time intervals of 0.5 Myr (from top left to top right to bottom left to bottom right). The figure demonstrates the rapid changes in $\zeta_2(\nu_i)$ for the modes undergoing avoided crossings. The top-right model corresponds to the best-fit stellar model shown in Figures 6d and 10a. The bottom-left model provides a good match to observed $\zeta_2(\nu_i)$ (see Figure 10a); however, the chi-square for the seismic frequencies is much higher than that of the best-fit model shown in the top right.